Accepted manuscript at https://doi.org/10.1098/rsif.2021.0871

A predictive multiscale model of in-stent restenosis in femoral arteries: linking hemodynamics and gene expression with an agent-based model of cellular dynamics

Anna Corti[1], Monika Colombo[1,2], Jared M. Rozowsky[3], Stefano Casarin[4,5,6], Yong He[3], Dario Carbonaro[7], Francesco Migliavacca[1], Jose F. Rodriguez Matas[1], Scott A. Berceli[3,8], Claudio Chiastra[1,7]

1. LaBS, Department of Chemistry, Materials and Chemical Engineering "Giulio Natta", Politecnico di Milano, Milan, Italy
2. Institute for Chemical and Bioengineering, Department of Chemistry and Applied Biosciences, ETH Zürich, Switzerland
3. Department of Surgery, University of Florida, Gainesville, FL, USA
4. Department of Surgery, Houston Methodist Hospital, Houston, TX, USA
5. Center for Computational Surgery, Houston Methodist Research Institute, Houston, TX, USA
6. Houston Methodist Academic Institute, Houston, TX, USA
7. PoliTo^{BIO}Med Lab, Department of Mechanical and Aerospace Engineering, Politecnico di Torino, Turin, Italy
8. Malcom Randall VAMC, Gainesville, FL, USA

***Address for correspondence:**

Claudio Chiastra, PhD

PoliTo^{BIO}Med Lab, Department of Mechanical and Aerospace Engineering

Politecnico di Torino, Corso Duca degli Abruzzi 24, 10129 Turin, Italy

claudio.chiastra@polito.it

Accepted manuscript at https://doi.org/10.1098/rsif.2021.0871

Abstract

In-stent restenosis (ISR) is a maladaptive inflammatory-driven response of femoral arteries to percutaneous transluminal angioplasty and stent deployment, leading to lumen re-narrowing as consequence of excessive cellular proliferative and synthetic activities. A thorough understanding of the underlying mechanobiological factors contributing to ISR is still lacking. Computational multiscale models integrating both continuous- and agent-based approaches have been identified as promising tools to capture key aspects of the complex network of events encompassing molecular, cellular and tissue response to the intervention. In this regard, this work presents a multiscale framework integrating the effects of local hemodynamics and monocyte gene expression data on cellular dynamics to simulate ISR mechanobiological processes in a patient-specific model of stented superficial femoral artery. The framework is based on the coupling of computational fluid dynamics simulations (hemodynamics module) with an agent-based model (ABM) of cellular activities (tissue remodeling module). Sensitivity analysis and surrogate modeling combined with genetic algorithm optimization were adopted to explore the model behavior and calibrate the ABM parameters. The proposed framework successfully described the patient lumen area reduction from baseline to 1-month follow-up, demonstrating the potential capabilities of this approach in predicting the short-term arterial response to the endovascular procedure.

Keywords

Lower-limb peripheral arteries, restenosis, multiscale modeling, agent-based modeling, computational fluid dynamics, mechanobiology

1. Introduction

Peripheral artery disease (PAD) is an atherosclerosis-related disease affecting more than 230 million people worldwide [1]. PAD mainly occurs in lower limb arteries, predominantly in the superficial femoral artery (SFA) [2]. Percutaneous transluminal angioplasty (PTA) with self-expanding stent implantation is a common endovascular treatment of atherosclerotic SFAs [3]. However, its long-term success is often compromised by the occurrence of in-stent restenosis (ISR), characterized by exacerbated smooth muscle cell (SMC) activity leading to excessive neointimal growth and subsequent lumen re-narrowing [4]. In the SFA the ISR incidence rate ranges between 15% and 32% [5].

ISR and vascular adaptation processes are driven by complex, multifactorial and multiscale networks of events involving feedback mechanisms, cause-effect relationships and mutual interactions of components at different spatio-temporal scales, from molecular (e.g., gene pattern alteration) to cellular and tissue/organ ones [6]. Among the heterogeneous factors favoring ISR, the vessel wall damage-related inflammatory response induced by stent implantation and the stent-related hemodynamic alteration play significant roles [4]. The lack of a thorough understanding of ISR mechanobiological mechanisms has fostered an extensive in-vitro, in-vivo and in-silico research aimed to provide insights in the process. In this context, in-silico multiscale models inspired by systems biology principles have been recently proposed to investigate the underlying mechanisms of ISR [6]. Different modeling strategies, based on continuum (e.g., [7,8]) and/or discrete (e.g., [9]) approaches, have been adopted [6]. Among these, multiscale agent-based modeling frameworks, integrating both continuous- and agent-based approaches, has emerged as promising tools being able to (i) include components across molecular, cellular and tissue scales, and (ii) capture the dynamic interplay of mechanobiological events responding to stent implantation [6].

The available multiscale frameworks have mainly described the cellular events and the subsequent arterial wall remodeling triggered by the intervention-induced damage and/or hemodynamic alteration in idealized vessel geometries [6]. However, patient-specific applications are lacking. Furthermore, multi-omics data (e.g., gene expression data, protein networks) have not been integrated in these frameworks yet, although deemed to be the future target of cardiovascular medicine [10]. Recently, monocyte gene expression analysis has enabled the identification of markers of systemic inflammation (target genes) associated with the clinical success/failure of PTA and stenting of femoral arteries [11]. Its integration into an in-silico framework will allow to better elucidate the ISR mechanisms and contribute to improve the management of PAD.

Accordingly, this work presents a novel multiscale framework that integrates the effects of local hemodynamics and monocyte gene expression on cellular dynamics to simulate ISR mechanobiological processes in a patient-specific model of stented SFA. The framework consists of a computational fluid dynamics (CFD) simulation (hemodynamics module) coupled with an agent-based model (ABM) of cellular dynamics (tissue remodeling module). The model replicates cellular behaviors and arterial wall remodeling in response to the CFD-derived hemodynamic input and the inflammatory cues (monocyte gene expression data), triggered by stenting. Sensitivity analysis and surrogate modeling were adopted to explore the model behavior and calibrate the ABM parameters respectively. To assess the framework feasibility and verify its capability to describe the short-term arterial response to the endovascular procedure, the framework was applied to one patient-specific case and the simulated lumen area reduction at 1 month was compared with the patient's follow-up data.

2. Methods

2.1 Patient-specific multiscale framework

Figure 1 schematizes the patient-specific multiscale framework of ISR. The framework receives as input the patient-specific stented SFA three-dimensional (3D) geometry (i.e., post-intervention condition), the blood velocity waveform and the longitudinal data of patient's monocyte gene expression. The framework returns the 1-month follow-up 3D lumen geometry. The framework sees two coupled modules: (i) a hemodynamics and (ii) a tissue remodeling module. Within the first, the fluid domain of the 3D stented SFA is meshed and a steady-state CFD simulation is performed. The wall shear stress (WSS) profiles are extracted at several cross-sectional planes in the stented portion and given as input to the tissue remodeling module, which simulates the arterial adaptation in response to the intervention-induced local hemodynamic and the systemic inflammatory cues. Within the tissue remodeling module, a bidimensional (2D) ABM, implemented for each plane, replicates the cellular and extracellular matrix (ECM) dynamics leading to the overall arterial wall remodeling. At the end of the ABM simulations, corresponding to a 1-month period, the 3D lumen geometry is reconstructed from the ABM lumen contour of the simulated planes. The framework is fully automated and executed through an external subroutine in Matlab (MathWorks, Natick, MA, USA).

2.1.1. Clinical data

Fourteen patients who underwent PTA with stenting at the Malcom Randall VAMC (Gainesville, FL, USA) between 2007 and 2012 were selected to measure the monocyte gene expression. All patients were treated with self-expanding EverFlex stent (EV3, Medtronic, Dublin, Ireland). Blood samples were collected at 1 hour pre-intervention, and 2 hours, 1, 7, and 28 days post-intervention to perform monocyte gene expression analysis. Framework feasibility was assessed with a

one-patient pilot study. The patient was a 57-years old male, treated with a 40-mm long stent, and presented both computer tomography (CT) and Doppler ultrasound images at 1-week (baseline condition) and 1-month follow-up. The study was approved by the Institutional Review Board at the University of Florida (Gainesville, FL, USA) and conformed to the Helsinki Declaration on human research of 1975, as revised in 2000.

2.1.2. Monocyte gene expression analysis

Monocytes were isolated using a RosetteSep negative selection kit (StemCell Technologies, Vancouver, BC, Canada). RNA was isolated using RNeasy MiniKit and the quality assessed with an Agilent Bioanalyzer. cDNA was created using Ovation Pico WT kit (NuGEN, San Carlos, CA) and labeled with GeneChip WT Terminal Labeling (Affymetrix, Santa Clara, CA). The Glue Grant Human Transcriptome Array (GGH2, Affymetrix) [12] was used to measure the expression level of 34,834 genes and the raw expression data were normalized with Partek Genomics Suite (Partek, St. Louis, MO) for statistical analysis. Two-way analysis of variance (ANOVA) test was applied to identify the time-dependent genes (1,263 genes, $p<0.05$). A custom clustering algorithm [13] was adopted to group genes with similar dynamics. Accordingly, the 1,263 time-dependent genes were divided into 34 clusters. Moreover, a selection process was applied to detect the clusters that were most likely associated with the procedure outcome, namely the clinical success/failure at 1 year. Specifically, the clinical failure was defined as angiographic or Doppler ultrasound evaluation demonstrating occlusion or high-grade stenosis (greater than a 3.5-fold increase in peak systolic velocity) at the site of intervention, an associated interval decrease in ankle-brachial index (ABI)>15% with return of clinical symptoms, or the need for a secondary intervention of the index lesion [11]. The selection process was

based on four criteria: (i) significant ($p<0.05$) outcome difference identified by the clustering algorithm (24 clusters); (ii) significant ($p<0.05$) outcome difference identified by ANOVA (10 clusters); (iii) normalized Cohen d effect size at any time point between outcome groups>0.8 (10 clusters) and (iv) expression fold change at any time point from pre-operative condition<0.7 or >1.4 (3 clusters). As a result of the clustering and selection processes, 3 clusters containing 22 genes were found to be differentially expressed between the outcome groups, and thus potentially able to discriminate between 1-year clinical success/failure (Fig. 2). Specifically, the failure group was associated with a downregulation of cluster 5 genes and an upregulation of clusters 8 and 24 genes. The patient's gene expression profile of the three clusters (Fig. 2, red curves) was considered to represent the patient's systemic inflammation level and was assumed to contribute to the overall restenosis process, by influencing cellular dynamics in the ABM of tissue remodeling (detailed in Section 2.1.5).

2.1.3. Three-dimensional superficial femoral artery model

A previously developed semi-automatic method [14] was applied to reconstruct the patient-specific 3D vessel lumen geometry at baseline and 1-month follow-up. Since the CT images presented poor resolution and metallic artifacts, the stent struts were invisible, and a direct reconstruction of the stent was impossible. Hence, a 40-mm long EverFlex stent model was virtually implanted in the baseline model through a morphing procedure [15] using the mesh manipulation tool HyperMorph, available in HyperMesh (Altair Engineering, Troy, MI, USA) (Fig. 3A). The correct position of the stent model within the vessel was determined by the stent edges visible on CT. Additional morphing procedure details are reported in Supplementary Materials. The baseline stented SFA model was used to provide the framework initial condition, while the 1-month SFA model was used for its calibration.

2.1.4. Hemodynamics module

The baseline 3D stented SFA model was meshed using polyhedral elements and five boundary layers of prism elements near the wall (Fig. 3B). Curvature- and proximity-based refinement criteria were adopted to capture the stent-lumen intersection with a level of accuracy required for the generation of the ABM planes. Accordingly, a mesh sensitivity analysis, based on both the hemodynamic output and the ABM generation was performed, and the resulting mesh (~3,000,000 elements) was used in the framework. A steady-state CFD simulation was performed in the baseline stented SFA model (Fig. 3C). The boundary conditions were based on our previous studies [14,16,17]. Briefly, a parabolic velocity profile, with mean velocity derived from patient's Doppler ultrasound images (0.05 m/s corresponding to a flow-rate of 246 mL/min), was applied at the inlet; a flow-split of 0.67:0.33 was prescribed at the SFA and profunda femoris artery outlets, respectively; a no-slip condition was specified at the walls, considered as rigid. Blood was modeled as a non-Newtonian Carreau fluid with a density of 1060 kg/m^3 [14]. Details about the solver settings are reported in the Supplementary Materials. The software Fluent (Ansys Inc., Canonsburg, PA, USA) was employed for both the meshing and CFD simulation. To perform the subsequent ABM analysis, WSS profiles were extracted at 9 cross-sectional planes (1 plane every 2 stent rings) within the stented portion (the region of interest). This choice ensured the best compromise between computational costs and accuracy of the 3D surface reconstruction from the ABM outputs.

2.1.5. Tissue remodeling module

A 2D ABM, based on our work on atherosclerosis [18,19], was developed in Matlab to simulate, for each of the 9 planes, the 1-month follow-up arterial wall remodeling in response to patient-specific local hemodynamic and systemic gene expression stimuli.

The 2D ABM rests on a 300x300 site hexagonal grid (Fig. 3D). The initial configuration was generated by reconstructing the lumen wall and the stent struts from the 3D coordinates, after proper scaling, rotation and translation operations, needed to fit the ABM of the arterial wall within the computational grid. Specifically, a 0.0375 mm/site scale factor was adopted, so that each ABM site corresponds to ~1.5 cells (SMC diameter ~25 μm [20]). Intima, media and adventitia were generated according to literature thickness values of human femoral arteries [21,22] (Table 1). The internal elastic lamina (IEL) shape was assumed to mirror the lumen wall contour, while the external elastic lamina (EEL) and the vessel border were assumed as circular. The ABM was seeded with stent strut agents, SMCs and ECM (collagen and elastin) in the intima and in the media, and fibroblasts and collagen in the adventitia with previously adopted densities [18].

The ABM was initialized with WSS- and gene expression-based inputs (*WSSinput* and *GEinput*, respectively). *WSSinput* was set to reflect the emerging evidence of inverse relationship between the WSS and ISR, according to which low WSS promotes ISR [23]. Indeed, low WSS enhances SMC proliferative and synthetic activity both directly and through endothelial-mediated mechanisms, namely by contributing to a condition known as endothelial dysfunction characterized, among all, by altered nitric oxide release affecting SMC activity. Accordingly, each lumen wall ABM site was initialized with the corresponding CFD-derived WSS, from which a variable representing the level of endothelial dysfunction D was computed according to a sigmoid shaped curve defined as follows (Supplementary Fig. S1):

$$D(WSS)^i = -\frac{1}{1+e^{L_1(WSS^i - L_2)}} + 1 \quad (1)$$

where WSS^i is the WSS value at the i-th site of the lumen wall, and L_1 and L_2 are parameters defining the slope and the WSS value at which $D = 0.5$, respectively. D can assume values between 0 and 1, with higher levels of endothelial dysfunction associated with low WSS. As in [18], the primary endothelial lesion D, computed at the lumen wall sites, triggers a perturbation state that diffuses throughout the entire intima layer influencing intimal agent dynamics. *WSSinput* is thus constituted by (i) lumen wall sites endothelial dysfunction D and (ii) resulting intimal sites perturbation level, and is expressed as:

$$WSSinput = \begin{cases} D^i & lumen\ wall\ sites \\ \sum_i D(WSS)^i \times Amp \times \left(1 + \cos\left(\pi \frac{x}{dist}\right)\right) & intima\ sites \end{cases} \quad (2)$$

with $WSSinput \in [0\ 1]$. Specifically, *WSSinput* in the intima, at a distance $x<dist$ from the lumen wall (i-th sites), was computed as the sum of the decays of D, described as the cosine curve portion with negative slope and defined by the parameter *Amp*, amplitude of the cosine function.

Regarding *GEinput*, patient's monocyte gene expression curves (red curves in Fig. 2) and the average success curves of the 3 selected clusters (black curves in Fig. 2 - success group) were considered to formulate a patient-specific weight of the systemic inflammatory level. First, a generic inflammatory curve, inspired from literature [24], was generated (Fig. 4A), presenting a rapid increase in the first post-operative days (peak around day 2 [25]), followed by a rapid and then slow decay, vanishing after 1 month (in accordance with the monocyte gene expression curves). Second, for each cluster, the difference between the patient-specific curve and the average success curve was computed. Third, it was assumed that the more the patient-specific curve of the cluster deviates from the average success curve (towards the failure direction), the greater the inflammatory level (Supplementary Fig.

S2A). Accordingly, for each cluster a weight *w* was computed as a sigmoid-shaped function of the above defined difference (Supplementary Fig. S2B):

$$w_5 = -\frac{1}{1+e^{p_{ge}*\Delta_5}} + 1 \quad (3)$$

$$w_8 = \frac{1}{1+e^{p_{ge}*\Delta_8}} \quad (4)$$

$$w_{24} = \frac{1}{1+e^{p_{ge}*\Delta_{24}}} \quad (5)$$

where Δ_5, Δ_8 and Δ_{24} are the differences between the patient-specific curve and average success curve for the clusters 5, 8 and 24, respectively, and p_{ge} is a coefficient defining the slope of the sigmoid function. According to Eqs. 3-5, the more negative Δ_5 is, and the more positive Δ_8 and Δ_{24} are, the greater the inflammatory weights, since the patient-specific curves approach the failure one (Supplementary Fig. S2). The *GEinput* was thus computed as:

$$GEinput(t) = w_{tot} \times Inflammation(t - delay) \quad (6)$$

where w_{tot} is the product of the three cluster-specific weights, *Inflammation(t)* is the generic inflammatory curve in Fig. 4A and *delay* is the time period that was assumed for the activation of the cellular and ECM response to the inflammatory stimulus. In accordance with previous animal findings [26], *GEinput* was translated of 3 days to reproduce this delayed effect (Fig. 4B). To summarize, differently from *WSSinput*, which locally influences cellular activities, *GEinput* is associated with the systemic inflammatory response, thus constituting a trigger to all the intimal agents (i.e., all the cells/ECM intimal components are equally affected by *GEinput*).

Each agent was initialized with a random even number, representing the internal clock (i.e., the biological time), between 0 and T_{agent} (T_{cell}=24 hours [27] and T_{ECM}=4 hours [28], representing the agent biological cycle), ensuring the desynchronization of cellular activities. After the initialization

phase, the ABM performs the cellular activities, followed by proper geometrical regularization, with a 2 hour-time step over a 1-month period. At each time step, the agents reaching the end of their biological cycle (i.e., internal clock=T_{agent}) are identified as potentially active agents (i.e., ready for a biological event). The potentially active agents are randomly interrogated and the occurrence of a biological event is assessed. Specifically, for each potentially active agent, a random number between 0 and 1 is generated and compared with the agent probability of mitosis/apoptosis (for cell agents only), or ECM production/degradation (for cell and ECM agents) [18]. If the agent probability associated with the biological event (mitosis/apoptosis or ECM production/degradation) is greater than the randomly generated number, then the potentially active agent is upgraded to active agent and the specific biological event occurs. The baseline probabilities for cell mitosis/apoptosis and ECM production/degradation were set as in [18] and applied to the media and adventitia dynamics. In the intima, cell mitosis and ECM production were perturbed depending on *WSSinput* and *GEinput* of each agent *h*, as expressed in Eqs.7-8:

$$p^h_{division} = \alpha_1 + \alpha_2 WSSinput^h + \alpha_3 GEinput^h \quad (7)$$

$$p^h_{ECMproduction} = \alpha_4 + \alpha_5 WSSinput^h + \alpha_6 GEinput^h \quad (8)$$

α_1 and α_4 were set to 0.05 and 0.008, respectively [18]. α_2, α_3, α_5 and α_6, weighing the effects of hemodynamics and systemic inflammation on cell mitosis or ECM production, were calibrated as explained in Section 2.2. Once the active agents are determined, they are randomly accessed, the specific biological event is replicated and the internal clock of both the newly formed agent (in case of mitosis or ECM production) and the active one is reset.

Cell mitosis and ECM production imply the addition of a new agent next to the active one, while cell apoptosis and ECM degradation the removal of the active agent. Agent dynamics in the

intima are inward-oriented while those in the media and adventitia are outward-oriented. The details of tissue reorganization at event occurrence are reported in [18]. Finally, regularization algorithms were applied at each time step to guarantee the preservation of smooth contours. Specifically: (i) at the lumen wall, agents were locally redistributed to maximize their contact; (ii) the IEL was reinitialized to its initial configuration; and (iii) the EEL and the external border were redefined as circles with their current average radii.

Due to the ABM stochasticity, 3 simulations were performed for each plane starting from the same initial condition. The lumen coordinates obtained from the 3 simulations were collected and the lumen contour minimizing the root mean square deviation from the average one was selected for each plane [18]. Finally, the 1-month follow-up 3D arterial lumen geometry was obtained by lofting the selected lumen contour of the ABM planes using Rhinoceros (Robert McNeel & Associates, Seattle, WA, USA).

2.2 Sensitivity analysis, surrogate modeling and calibration

A preliminary sensitivity analysis was performed on a single ABM plane to identify the parameters that mainly govern the ABM outputs, reducing the total number of parameters to be calibrated and thus the computational efforts. Then, surrogate modeling of tissue remodeling module was adopted to define an approximate relationship between selected ABM parameters and the global outputs of interest referred to the resulting follow-up arterial configuration in the stented portion, namely the 1-month lumen area and the normalized intimal ECM/SMC ratio (ECM/SMC_{ratio_int}). The surrogate models were (i) used to explore the relation between the ABM parameters and the global

outputs, and (ii) employed in the calibration process, in which the selected ABM parameters were calibrated through genetic algorithm optimization.

2.2.1 Preliminary sensitivity analysis

A set of j=8 ABM parameters $\{\alpha_2, \alpha_3, \alpha_5, \alpha_6, L_1, L_2, Amp$ and $p_{ge}\}$, with ranges reported in Table 2, was considered. In particular, the range of L_1, L_2 was set to satisfy a 10% tolerance on the value of D, meaning that $D(WSS=0)>0.9$ and $D(WSS=1)<0.1$. Similarly, a 10% tolerance criterion was considered to set the range of p_{ge}, so that $w_5(\Delta=1)<0.1$, $w_5(\Delta=-1)>0.9$, $w_{8,24}(\Delta=1)>0.9$ and $w_{8,24}(\Delta=-1)<0.1$, with $\Delta=\pm1$ being extreme values for the patient-specific case. The ranges of α_2, α_3, α_5, α_6, and Amp were defined by running extreme case scenarios (i.e., $WSSinput=1$ and $GEinput=0.7$, which represented the maximum possible values for the investigated patient) and choosing upper limits that guaranteed successful 1-month ABM simulations. Latin hypercube sampling (LHS) was adopted to sample the admissible range of the j parameters in k=1000 equal intervals, needed to achieve statistical significance in the sensitivity analysis. A LHS matrix ($k\times j$) was obtained, identifying k parameter combinations [18,29]. Since all the planes presented similar $WSSinput$ (i.e., WSS<0.4 Pa) and identical $GEinput$ the analysis was performed on a single ABM plane, being the aim of the analysis that of obtaining a generic relationship between the ABM parameters and the output. Plane 2 was selected for the analysis because it presented the lowest WSS, thus allowing exploring the extreme case scenario. Partial rank correlation coefficients (PRCCs) were computed in Matlab to measure the correlation between each ABM parameter and the ABM outputs of interest (i.e., the 1-month ABM lumen area, and the intimal cell and ECM content, normalized by the initial value) [18,29]. Statistically significant correlations were assumed for p-value<0.05.

2.2.2 Surrogate modeling

A Gauss process surrogate model of the tissue remodeling module was developed in Matlab for each global outputs, namely (i) the median lumen area of the stented portion and (ii) the normalized ECM/SMC_{ratio_int}, both referred to the resulting follow-up arterial configuration, and computed as detailed in the Supplementary Materials. Only the n ($\leq j$) ABM parameters that were found to be significantly correlated with the ABM outputs in the preliminary sensitivity analysis were considered to build the two surrogate models. To construct them, s=10×n samples were generated through LHS (training data set). Specifically, a LHS matrix (s×n) was obtained by dividing the range of the n=6 {α_2, α_3, α_5, α_6, Amp and p_{ge}} ABM parameters (see Section 3.1 for the results of the preliminary sensitivity analysis, identifying 6 significantly correlated parameters) in s=60 equal intervals, and s parameter combinations were obtained. Parameters L_1, L_2 were maintained constant at their half range values (i.e., L_1=-15.25 and L_2=0.5). For each parameter combination s, the tissue remodeling module (consisting in 3 ABM simulations of the 9 planes and the 1-month 3D arterial lumen geometry reconstruction) was run, and the median lumen area of the stented portion and the normalized ECM/SMC_{ratio_int} were computed. The surrogate models were validated by: (i) applying the leave-one-out method; and (ii) using a validation set of 10 samples, chosen to span over the possible entire range of lumen area (considering the parameter range reported in Table 2) [30]. The consistency between the predicted and simulated outputs was assessed in the leave-one-out process by plotting the predicted outputs as a function of the simulated ones and then evaluating the coefficient of determination R^2_{pred}, and by computing the standardized cross validated residual (SCVR) values [30]. The R^2_{pred} between the predicted and simulated outputs was also quantified in the case of the validation set [30].

2.2.3 Calibration

To calibrate the ABM parameters, an optimization problem was defined so that the optimal *n* parameters within their admissible range could: (i) minimize the difference between the median lumen area of the stented portion of the model and that measured in-vivo at 1 month; and (ii) guarantee a normalized $ECM/SMC_{ratio\_int} \in [0.5\ 1.5]$. Based on the available clinical data, the patient 1-month lumen area was the only comparative information usable in the calibration process. Moreover, a constraint on the normalized ECM/SMC_{ratio_int} was set to prevent excessive unbalanced neointima composition, with respect to the baseline condition. Indeed, both increased SMC and/or ECM content may be observed in neointimal ISR tissue. However, the predominant content of cells or ECM depends on the subject and the post-procedural time [31,32]. Accordingly, as conservative hypothesis, no extreme temporal changes in the ECM/SMC_{ratio_int} were assumed as detailed below. Mathematically, the objective and constraint functions were defined as:

$$f_{LA}(\boldsymbol{x}) = \left| LA_{SM} - LA_{patient} \right| \tag{9}$$

$$f_{ECM/cell}(\boldsymbol{x}) = \left. \frac{ECM/cell|_{1\ month}}{ECM/cell|_{day\ 0}} \right|_{SM} \tag{10}$$

where $\boldsymbol{x}$ is the vector of the ABM parameters; $f_{LA}(\boldsymbol{x})$ is the optimization objective, with LA_{SM} and $LA_{patient}$ being the 1-month median lumen area of the stented portion predicted by the surrogate model and measured on the patient, respectively; and $f_{ECM/cell}(\boldsymbol{x})$ is the constraint, computed as the 1-month normalized ECM/SMC_{ratio_int} predicted by the surrogate model. Within the optimization process, the two surrogate models were thus interrogated through the definition of the objective and constraint functions. The single, constrained optimization problem was written as:

$$\begin{cases} \underset{\boldsymbol{x} \in A}{min}\, f_{LA}(\boldsymbol{x}) \\ s.t: \begin{cases} 0.5 < f_{ECM/cell}(\boldsymbol{x}) < 1.5 \\ A = \begin{Bmatrix} \boldsymbol{x} = [\alpha_2, \alpha_3, \alpha_5, \alpha_6, Amp, p_{ge}]: \ \alpha_2 \in [0, 0.1], \alpha_3 \in [0, 1.7], \alpha_5 \in [0, 1.77], \\ \alpha_6 \in [0, 0.1], Amp \in [0.013, 0.13], p_{ge} \in [-6, -2.5] \end{Bmatrix} \end{cases} \end{cases} \quad (11)$$

The non-dominated sorting genetic algorithm (NSGA-II) was adopted in Matlab to find the optimal solution. The settings of the algorithm are reported in the Supplementary Materials. Finally, the resulting optimum parameters were set in the ABM and the tissue remodeling module was run to assess the goodness of the calibration procedure.

3. Results

3.1. Preliminary sensitivity analysis

The PRCCs between the j=8 ABM parameters and the 3 ABM outputs of interest, normalized by their initial values, are illustrated in Fig. 5. Six out of 8 parameters (i.e., α_2, α_3, α_5, α_6, *Amp* and p_{ge}) presented significant PRCCs with all investigated outputs and hence were identified as the driving ABM parameters. Since the remaining 2 parameters (L_1 and L_2) were not correlated with any output, they were excluded from the subsequent global sensitivity analysis (i.e., parameter exploration through the surrogate models referred to the follow-up arterial configuration) and calibration process, reducing the associated computational costs without affecting the output validity.

The 6 parameters exhibiting significant PRCCs were all negatively correlated with the final lumen area, with *Amp* presenting the highest negative correlation. Moreover, among the agent probability parameters (α_2, α_3, α_5, α_6), (i) those associated with the *WSSinput* (α_2, α_5) were more strongly correlated with the final lumen area than those multiplying the *GEinput* in the same probability equation (α_3, α_6), and (ii) the parameters governing the ECM production (α_5, α_6) affected

more the final lumen area than the dual ones in the SMC proliferation probability equation (α_2, α_3). The same considerations held for the final intimal ECM content, but with positive PRCCs. As expected, higher α_5, α_6, *Amp* and p_{ge} lead to increased ECM content, being α_5 and α_6 the direct driver of ECM production in the intima, and *Amp* and p_{ge} associated with the *WSSinput* and *GEinput*, respectively. Moreover, α_2 and α_3, by directly driving SMC proliferation, had a role in the ECM production since ECM deposition is mediated by the cell agents in the ABM. Accordingly, the higher the cellular content, the more ECM production is promoted. Finally, regarding the SMC content, positive correlations were found for α_2, α_3, *Amp* and p_{ge}, as expected. Conversely, negative correlations were found for α_5 and α_6, highlighting a counterintuitive behavior of the ABM for which an increase in α_5 and α_6 (promoting ECM production) leads to reduced cellularity.

3.2. Surrogate modeling: validation and parameter exploration

Sixty samples (i.e., derived from 60 combinations of the 6 previously identified driving ABM parameters), corresponding to 60 1-month arterial configurations (stented portion), were defined through LHS to build the surrogate models (training set). The 60 samples in terms of distributions of 1-month lumen area of the stented portion and normalized ECM/SMC_{ratio_int} are shown in Fig. 6. The median values of these distributions were considered for the generation of the surrogate models, as detailed in Section 2.2.2.

The outputs of the surrogate model validation procedure, based on the leave-one-out principle and 10 additional simulations, are presented in Fig. 7 and Supplementary Fig. S3. In both analyses, the surrogate model predictions and the simulated values of the 1-month lumen area and normalized ECM/SMC_{ratio_int} exhibited an excellent agreement, as supported by the high values of R^2_{pred} (Fig. 7).

Furthermore, in the leave-one out principle the SCVR values of the surrogate model predictions lied within the required interval [-3, 3] (Supplementary Fig. S3) [30], thus confirming the validity of the surrogate models.

The validated surrogate models were used to investigate the influence of each parameter on the two outputs of interest (i.e., 1-month lumen area and normalized ECM/SMC_{ratio_int}) by varying 3 parameters at a time while maintaining the others fixed at their half-range values (Fig. 8). The parameters were grouped based upon the association with *WSSinput* (i.e., α_2, α_5, Amp) and *GEinput* (i.e., α_3, α_6, p_{ge}). Overall, the *WSSinput*-associated parameters had more impact on the model outputs than the *GEinput*-associated ones (Fig. 8). Regarding the final lumen area, as expected, increases in α_2 and α_5 led to a decrease in the lumen area by enhancing cell mitosis and ECM production, respectively, and their effect was more pronounced at higher levels of *Amp* (Fig. 8A). Similar considerations held for the effect of α_3, α_6 and p_{ge} on the final lumen area (Fig. 8B). Regarding the normalized ECM/SMC_{ratio_int}, the highest values were observed for concurrent decrease of α_2 and increase of α_5 and *Amp*, thus confirming the major impact of the hemodynamic-related parameters (Fig. 8C). Moreover, as also confirmed by the observed relation of α_2 and α_5, and of α_3 and α_6, the normalized ECM/SMC_{ratio_int} raised with enhanced ECM production and reduced cell proliferation (Fig. 8C-D). Finally, similarly to the effects on the lumen area, *Amp* amplified the impact of α_2 and α_5, and p_{ge} amplified that of α_3 and α_6, on the normalized ECM/SMC_{ratio_int} (Fig. 8C-D).

3.3. Calibrated patient-specific model

The calibration procedure (Section 2.2.3) provided the optimum parameters $\boldsymbol{x} = [\alpha_2, \alpha_3, \alpha_5, \alpha_6, Amp, p_{ge}]$ (Table 3) that minimized the objective function $f_{LA}(\boldsymbol{x})$=4.3×10^{-11},

guaranteeing an acceptable normalized ECM/SMC$_{ratio_int}$, $f_{ECM/cell}(\boldsymbol{x})$=1.3. The ISR framework was run with the computed optimum ABM parameters. The model was verified in terms of consistency with the rules, robustness and repeatability. Furthermore, the lumen geometry obtained at 1-month was compared with the patient's lumen geometry reconstructed at the same time point to evaluate the framework capability to capture the short-term arterial response after the calibration process.

The WSS distribution in the stented portion and the temporal evolution of 3 explanatory ABM planes (i.e., planes 1, 5 and 9) at day 0, 10, 20 and 30 are shown in Fig. 9A and Supplementary video. The temporal trends of the normalized lumen, intima, media and adventitia areas, intimal SMC and ECM content, and normalized ECM/SMC$_{ratio_int}$, resulting from the 3 repeated simulations of the planes 1, 5 and 9, are reported in Fig. 9, panels B-C-D-E, respectively. The planes experienced a similar lumen area reduction (~25%) and presented a homogenous distribution of intimal growth. The absence of focal restenosis was due to the small variability of the WSS, both circumferentially within the plane and longitudinally among the 3 considered planes. The temporal trends of Fig. 9 elucidate the presence of 4 phases in the ABM dynamics that reflected the *GEinput* (dashed black line in Fig. 9B), namely: (i) a primary slight activation attributable to the sole *WSSinput* (silent *GEinput*); (ii) intense response starting at day 3 (corresponding to the activation of the *GEinput*); (iii) growth attenuation (corresponding to the *GEinput* decay); and (iv) linear growth (corresponding to the constant *GEinput* phase). As expected, the intima was the only layer involved in the restenosis process, undergoing a 2.5-fold area growth, while the media and adventitia preserved their initial areas. Within the intima, both the ECM and SMC agents contributed to ISR, with the ECM increasing more than the SMC, as also demonstrated by the rise of the normalized ECM/SMC$_{ratio_int}$ over time (consistent with the 1-month normalized ECM/SMC$_{ratio_int}$ obtained from the calibration process, $f_{ECM/cell}(\boldsymbol{x})$=1.3). Finally, the

repeatability of the model is evincible from the small interquartile range (Fig. 9B) and the high similarity of the outputs resulting from the 3 repetitions of each plane (Supplementary Fig. S4). Similar considerations held for all the 9 planes, whose selected 1-month ABM outputs are depicted in Fig. 10A.

The 1-month lumen contour of the 9 planes were used to reconstruct the 1-month lumen surface of the stented portion (Fig. 10B-C). The obtained lumen geometry was compared with the patient-specific lumen geometries reconstructed from CT immediately after stenting and at 1 month (Fig. 11A). No significant differences were observed between the patient's 1-month lumen area and the model prediction (Fig. 11B). In both the simulated and the patient's cases, a significant lumen area reduction was found at 1 month with respect to the condition immediately after stenting ($p<0.05$). Overall, the calibrated model provided an excellent estimation of the 1-month lumen area of the stented portion (model lumen area of 23.85 [22.29 24.47] mm^2 and patient's lumen area of 23.61 [22.68 25.79] mm^2). However, the model was not fully able to capture the local lumen geometrical variability, especially at the proximal region of the stented portion where focal narrowing was detected at 1 month in the patient's case (Fig. 11A, dashed box).

4. Discussion

Previous cellular scale ABMs were successfully integrated with molecular/tissue scale continuum-models to investigate the arterial response to hemodynamic and mechanical stimuli post-stenting [33,34,43,35–42]. However, applications to patient-specific scenarios are lacking and multi-omics data have never been included within these models [6]. The present study constitutes the first attempt of including patient gene expression data in a multiscale agent-based modeling framework of vascular adaptation. Specifically, a patient-specific multiscale framework of ISR integrating inputs at

different spatio-temporal levels, namely the hemodynamics at the tissue level and the monocyte gene expression accounting for systemic inflammation after stenting, at the molecular level, was developed. The framework was used to model the short-term response after self-expanding stent placement in a human SFA. Following a calibration procedure, the framework successfully described the lumen area change from baseline to 1-month follow-up.

The gene expression data used herein embed information on the patient's early activation state of the systemic inflammatory system in response to PTA with stenting and, similarly to [11], were found to be associated with the 1-year clinical success or failure of the procedure (as defined in Section 2.1.2). These data were assumed, in combination with the hemodynamic stimuli, as key drivers of cellular dynamics and arterial adaptation after the endovascular intervention. However, given the lack of deeper ontological analysis, a direct association between specific genes and cellular activity was not possible. Accordingly, the main model assumption was that a pronounced and persistent inflammatory response (represented by *GEinput*) triggers a more intense and long-lasting cellular activity, resulting in intimal hyperplasia and ISR. This hypothesis agrees with the numerous studies demonstrating the relevant role of inflammation in restenosis and identifying biomarkers of systemic inflammation associated with restenosis (e.g., [11,25,44,45]). Furthermore, although the considered gene expression-based stimulus potentially encompasses several pro-inflammatory factors related to the overall intervention, it was supposed to be mainly associated to the arterial wall damage induced by PTA. Indeed, the PTA-provoked injury, consisting in endothelial denudation and potential arterial wall dissection, likely represents the major intervention-related trauma triggering the early inflammatory response [46]. Given the systemic nature of the gene expression data and being unable (due to the available data) to identify regions subjected to higher PTA-induced trauma, the *GEinput* was assumed

to equally influencing intimal cellular activities, thus constituting a global trigger to ISR. Consequently, the simulated process of ISR was overall governed by the systemic inflammatory response and locally modulated by the hemodynamics.

Previous multiscale agent-based modeling frameworks of ISR in idealized vessel geometries focused on the effect of local arterial wall damage induced by stenting on the ABM-simulated cellular behavior and ISR process [39–43]. In these studies, the authors (i) performed a finite element analysis of stent deployment and computed the arterial wall damage as function of the von Mises stress, (ii) modeled the damage-induced temporal variation of inflammatory variables (e.g., growth and matrix degrading factors) through a set of ordinary differential equations and (iii) implemented an ABM of cellular behaviors driven by the damage-induced inflammatory cues. In the present study, the pre-operative patient-specific vessel was completely obstructed, preventing us from performing a finite element analysis of PTA and stent deployment, and obtaining an estimation of local damage. Furthermore, in the previous idealized models [39,41–43] a key role was attributed to the re-endothelialization process, through the explicit modeling of endothelial cells and the definition of rules accounting for the inhibitory effect of the endothelial released nitric oxide on SMC activity. However, the hemodynamics was not computed and the WSS influence on the endothelial nitric oxide production was not modeled. In the studies by Hoekstra's research group [35–38], to reproduce the endothelium-mediated hemodynamic influence on SMCs, the probability of presence of functional endothelium over time was modeled without explicitly including endothelial cells and a literature-derived relation between nitric oxide endothelial production and WSS was used to drive SMC dynamics. In the present framework, the endothelial cells were not explicitly modeled. Instead, a phenomenological representation of the direct and indirect (endothelial-mediated) hemodynamic effects on SMC activity

was proposed. Each lumen wall agent was initialized with a variable accounting for the endothelial dysfunction, computed as function of the WSS, from which each intimal agent was then initialized with a variable (*WSSinput*) representing the overall hemodynamic-related trigger to SMC and ECM activity. Accordingly, *WSSinput* embedded, among all, the nitric oxide mediated mechanisms.

In this study, a feasible and effective workflow for the sensitivity analysis and calibration of the ABM of ISR was also presented, constituting fundamental phases of the modeling process towards the assessment of the model reliability. Besides Nikishova et al. [47], in which a robust sensitivity analysis and uncertainty quantification were performed, in the previously cited multiscale ISR models [33,34,43,35–42], the model response was solely analyzed by tuning few clinically relevant parameters (e.g., stent strut thickness, re-endothelialization rate) to assess the model capability in identifying intervention-related factors affecting the procedure outcome. Here, the preliminary sensitivity analysis performed on the ABM, based on PRCC evaluation, allowed identifying the driving ABM parameters. This, besides providing insights into the ABM working mechanisms, was useful for the calibration process. Indeed, the calibration of all the ABM parameters in a single-step process through the evaluation of the lumen area and the normalized ECM/SMC_{ratio_int} as outputs may result not only computationally expensive, but also ineffective. Hence, focusing the calibration problem only on those parameters that mainly drive the ABM outputs allowed reducing the computational costs while maintaining the accuracy of the results high.

The combination of LHS with Gauss process surrogate model was successfully applied, enabling the formulation of metamodels of the tissue remodeling module that provide an estimate of the 1-month lumen area and normalized ECM/SMC_{ratio_int}. The surrogate models were used to explore the interrelation among the parameters and the ABM outputs. Moreover, through their interrogation

within the genetic algorithm optimization, the ABM parameters were successfully calibrated. Overall, the calibrated multiscale framework of ISR was able to replicate the patient's lumen area reduction at 1 month. However, some local geometrical features of the vessel were not captured by the simulation, suggesting that additional factors may play a role in the remodeling process.

This study has some limitations. As pilot study, only one patient-specific stented SFA lesion was modeled. This allowed assessing the feasibility and potentiality of the developed method. However, additional cases are required to validate the proposed computational framework and subsequently evaluate its applicability in the real-world clinical practice. As described above, the model was unable to fully capture the local heterogenous response of the artery to stenting. This could be partially attributed to two aspects. First, *GEinput*, being related to the systemic inflammation, was spatially uniform within the whole domain. The hemodynamic-related factor (*WSSinput*) was the only local input that could determine heterogenous growth patterns. Nevertheless, due to the little variability of the WSS (both circumferentially and longitudinally), a uniform intimal growth was obtained within all the planes. This suggests that additional inputs (e.g., the local arterial wall damage) should be considered. Second, given the unavailability of patient-specific data of arterial tissue composition, a uniform distribution of cells and ECM was assumed to model the ABM intima, media and adventitia layers. However, the real atherosclerotic vessel was probably composed by non-uniform tissue with plaque components (e.g., calcifications) that could likely lead to heterogeneous growth patterns. In this context, intravascular imaging techniques detecting the plaque composition (e.g., virtual-histology intravascular ultrasound or the combination of optical coherence tomography with near-infrared spectroscopy [48]) would allow determining additional lesion-specific features, besides improving the 3D vessel reconstruction. Last, in the present study only the short-term (i.e., 1-month) arterial response to stenting was simulated. Although

the first post-operative month was found to be the most dynamic one, being also affected by the early inflammatory response (as represented by the available monocyte gene expression data), the peak of restenosis was observed at 1 year in a study on stented SFAs [49]. Moreover, the dynamics of vessel remodeling during the first year after SFA stenting seems to be characterized by 3 main phases, namely: (i) fast lumen area reduction in the first post-operative month; (ii) slow lumen area change until 6 months; and (iii) potential focal restenosis after 6 months [16]. Given the clinical relevance of the long-term (e.g., 1-year) arterial response, in the future, the proposed computational framework will be adapted to investigate the vessel remodeling processes for longer post-intervention periods. In particular, a bi-directional coupling between the hemodynamics and the tissue remodeling modules will be performed to compute the hemodynamics in the current remodeled vessel geometry and consequently update the *WSSinput* to the ABM cellular activities, as previously done in [18]. In the long-term scenario, which can be characterized by focal restenosis and thus by larger intra- and inter-patient heterogeneity than the short-term period, the inclusion of patient comorbidities (e.g., diabetes and coronary artery disease) and lesion characteristics within the framework might be even more impactful in its predictive power.

5. Conclusions

The developed patient-specific multiscale framework of ISR simulated arterial wall remodeling following stent deployment intervention by integrating the effects of local hemodynamics and monocyte gene expression within an ABM of cellular dynamics. The multiscale framework was applied to a human stented SFA lesion. After proper calibration, the computational framework was able to describe the patient's lumen area reduction from baseline to 1-month follow-up. The overall results highlighted the potential capability of the mechanobiological model in predicting the short-term arterial response to the

endovascular procedure. In the future, the model will be validated on the other available patient-specific cases and its capability to predict the long-term outcome will be assessed.

Declarations

Funding

This work has been supported by Fondazione Cariplo, Italy (Grant number 2017-0792, TIME). FM and CC have been also partially supported by the Italian Ministry of Education, University and Research (FISR2019_03221, CECOMES).

Competing interests

The authors declare that they have no competing interests.

References

1. Song P, Rudan D, Zhu Y, Fowkes FJI, Rahimi K, Fowkes FGR, Rudan I. 2019 Global, regional, and national prevalence and risk factors for peripheral artery disease in 2015: an updated systematic review and analysis. *Lancet. Glob. Heal.* **7**, e1020–e1030. (doi:10.1016/S2214-109X(19)30255-4)

2. Kasapis C, Gurm HS. 2010 Current approach to the diagnosis and treatment of femoral-popliteal arterial disease. A systematic review. *Curr. Cardiol. Rev.* **5**, 296–311. (doi:10.2174/157340309789317823)

3. Katsanos K, Tepe G, Tsetis D, Fanelli F. 2014 Standards of practice for superficial femoral and popliteal artery angioplasty and stenting. *Cardiovasc. Intervent. Radiol.* **37**, 592–603. (doi:10.1007/s00270-014-0876-3)

4. Chaabane C, Otsuka F, Virmani R, Bochaton-Piallat ML. 2013 Biological responses in stented arteries. *Cardiovasc. Res.* **99**, 353–363. (doi:10.1093/cvr/cvt115)

5. Kim W, Choi D. 2018 Treatment of femoropopliteal artery in-stent restenosis. *Korean Circ. J.* **48**, 191–197. (doi:10.4070/kcj.2018.0074)

6. Corti A, Colombo M, Migliavacca F, Rodriguez Matas JF, Casarin S, Chiastra C. 2021 Multiscale computational modeling of vascular adaptation: A systems biology approach using agent-based models. *Front. Bioeng. Biotechnol.* **9**, 744560. (doi:10.3389/fbioe.2021.744560)

7. Escuer J, Martínez MA, McGinty S, Peña E. 2019 Mathematical modelling of the restenosis process after stent implantation. *J. R. Soc. Interface* **16**, 20190313. (doi:10.1098/rsif.2019.0313)

8. Maes L, Cloet A-S, Fourneau I, Famaey N. 2021 A homogenized constrained mixture model of restenosis and vascular remodelling after balloon angioplasty. *J. R. Soc. Interface* **18**, 20210068. (doi:10.1098/rsif.2021.0068)

9. Curtin AE, Zhou L. 2014 An Agent-Based Model of the Response to Angioplasty and Bare-Metal Stent Deployment in an Atherosclerotic Blood Vessel. *PLoS One* **9**, e94411. (doi:10.1371/journal.pone.0094411)

10. Ouzounian M, Lee DS, Gramolini AO, Emili A, Fukuoka M, Liu PP. 2007 Predict, prevent and personalize: Genomic and proteomic approaches to cardiovascular medicine. *Can. J. Cardiol.* **23 Suppl A**, 28A-33A. (doi:10.1016/s0828-282x(07)71003-6)

11. DeSart K, O'Malley K, Schmit B, Lopez MC, Moldawer L, Baker H, Berceli S, Nelson P. 2016 Systemic inflammation as a predictor of clinical outcomes after lower extremity angioplasty/stenting. *J. Vasc. Surg.* **64**, 766-778.e5. (doi:10.1016/j.jvs.2015.04.399)

12. Xu W *et al.* 2011 Human transcriptome array for high-throughput clinical studies. *Proc. Natl. Acad. Sci.* **108**, 3707–3712. (doi:10.1073/pnas.1019753108)

13. Wang Y, Xu M, Wang Z, Tao M, Zhu J, Wang L, Li R, Berceli SA, Wu R. 2012 How to cluster gene expression dynamics in response to environmental signals. *Brief. Bioinform.* **13**, 162–174. (doi:10.1093/bib/bbr032)

14. Colombo M, Bologna M, Garbey M, Berceli S, He Y, Rodriguez Matas JF, Migliavacca F, Chiastra C. 2020 Computing patient-specific hemodynamics in stented femoral artery models obtained from computed tomography using a validated 3D reconstruction method. *Med. Eng. Phys.* **75**, 23–35. (doi:10.1016/j.medengphy.2019.10.005)

15. Colombo M *et al.* 2022 Superficial femoral artery stenting: Impact of stent design and overlapping on the local hemodynamics. *Comput. Biol. Med.* , 105248. (doi:https://doi.org/10.1016/j.compbiomed.2022.105248)

16. Colombo M *et al.* 2021 In-Stent Restenosis Progression in Human Superficial Femoral Arteries: Dynamics of Lumen Remodeling and Impact of Local Hemodynamics. *Ann. Biomed. Eng.* **49**, 2349–2364. (doi:10.1007/s10439-021-02776-1)

17. Colombo M, He Y, Corti A, Gallo D, Casarin S, Rozowsky JM, Migliavacca F, Berceli S, Chiastra C. 2021 Baseline local hemodynamics as predictor of lumen remodeling at 1-year follow-up in stented superficial femoral arteries. *Sci. Rep.* **11**, 1613. (doi:10.1038/s41598-020-80681-8)

18. Corti A, Chiastra C, Colombo M, Garbey M, Migliavacca F, Casarin S. 2020 A fully coupled computational fluid dynamics – agent-based model of atherosclerotic plaque development: Multiscale modeling framework and parameter sensitivity analysis. *Comput. Biol. Med.* **118**, 103623. (doi:10.1016/j.compbiomed.2020.103623)

19. Corti A, Casarin S, Chiastra C, Colombo M, Migliavacca F, Garbey M. 2019 A Multiscale Model

of Atherosclerotic Plaque Development: Toward a Coupling Between an Agent-Based Model and CFD Simulations. In *Computational Science -- ICCS 2019* (eds JMF Rodrigues, PJS Cardoso, J Monteiro, R Lam, V V Krzhizhanovskaya, MH Lees, JJ Dongarra, PMA Sloot), pp. 410–423. Cham: Springer International Publishing.

20. Tahir H, Niculescu I, Bona-Casas C, Merks RMH, Hoekstra AG. 2015 An in silico study on the role of smooth muscle cell migration in neointimal formation after coronary stenting. *J. R. Soc. Interface* **12**, 20150358. (doi:10.1098/rsif.2015.0358)

21. Hafner NM, Womack CJ, Luden ND, Todd MK. 2016 Arterial adaptations to training among first time marathoners. *Cardiovasc. Ultrasound* **14**, 1–9. (doi:10.1186/s12947-016-0063-6)

22. Wong M, Edelstein J, Wollman J, Bond MG. 1993 Ultrasonic-pathological comparison of the human arterial wall. Verification of intima-media thickness. *Arterioscler. Thromb. A J. Vasc. Biol.* **13**, 482–486. (doi:10.1161/01.ATV.13.4.482)

23. Koskinas KC, Chatzizisis YS, Antoniadis AP, Giannoglou GD. 2012 Role of endothelial shear stress in stent restenosis and thrombosis: Pathophysiologic mechanisms and implications for clinical translation. *J. Am. Coll. Cardiol.* **59**, 1337–1349. (doi:10.1016/j.jacc.2011.10.903)

24. Edelman ER, Rogers C. 1998 Pathobiologic responses to stenting. *Am. J. Cardiol.* **81**, 4E-6E. (doi:10.1016/s0002-9149(98)00189-1)

25. Schillinger M, Exner M, Mlekusch W, Haumer M, Ahmadi R, Rumpold H, Wagner O, Minar E. 2002 Balloon angioplasty and stent implantation induce a vascular inflammatory reaction. *J. Endovasc. Ther. an Off. J. Int. Soc. Endovasc. Spec.* **9**, 59–66. (doi:10.1177/152660280200900111)

26. Jiang Z, Wu L, Miller BL, Goldman DR, Fernandez CM, Abouhamze ZS, Ozaki CK, Berceli SA. 2004 A novel vein graft model: adaptation to differential flow environments. *Am. J. Physiol. Heart Circ. Physiol.* **286**, H240-5. (doi:10.1152/ajpheart.00760.2003)

27. Cooper GM. 2000 *The Cell: A Molecular Approach. 2nd Edition*. American Society of Microbiology. ISBN-10: 0-87893-106-6 ISBN-13: 978-0-87893-106-4.

28. Hwang M, Garbey M, Berceli SA, Wu R, Jiang Z, Tran-Son-Tay R. 2013 Rule-based model of vein graft remodeling. *PLoS One* **8**, e57822. (doi:10.1371/journal.pone.0057822)

29. Marino S, Hogue IB, Ray CJ, Kirschner DE. 2008 A methodology for performing global uncertainty and sensitivity analysis in systems biology. *J. Theor. Biol.* **254**, 178–196. (doi:10.1016/j.jtbi.2008.04.011)

30. Carbonaro D, Gallo D, Morbiducci U, Audenino A, Chiastra C. 2021 In silico biomechanical design of the metal frame of transcatheter aortic valves: multi-objective shape and cross-sectional size optimization. *Struct. Multidiscip. Optim.* **64**, 1825–1842. (doi:10.1007/s00158-021-02944-w)

31. Chung IM, Gold HK, Schwartz SM, Ikari Y, Reidy MA, Wight TN. 2002 Enhanced extracellular matrix accumulation in restenosis of coronary arteries after stent deployment. *J. Am. Coll. Cardiol.* **40**, 2072–2081. (doi:10.1016/S0735-1097(02)02598-6)

32. Kearney M, Pieczek A, Haley L, Losordo DW, Andres V, Schainfeld R, Rosenfield K, Isner JM. 1997 Histopathology of in-stent restenosis in patients with peripheral artery disease. *Circulation* **95**, 1998–2002. (doi:10.1161/01.CIR.95.8.1998)

33. Caiazzo A *et al.* 2011 A Complex automata approach for in-stent restenosis: two-dimensional multiscale modelling and simulations. *J. Comput. Sci.* **2**, 9–17. (doi:10.1016/j.jocs.2010.09.002)

34. Tahir H, Hoekstra AG, Lorenz E, Lawford P V., Hose DR, Gunn J, Evans DJW. 2011 Multi-scale simulations of the dynamics of in-stent restenosis: impact of stent deployment and design. *Interface Focus* **1**, 365–373. (doi:10.1098/rsfs.2010.0024)

35. Tahir H, Bona-Casas C, Hoekstra AG. 2013 Modelling the effect of a functional endothelium on the development of in-stent restenosis. *PLoS One* **8**, e66138. (doi:10.1371/journal.pone.0066138)

36. Tahir H, Bona-Casas C, Narracott AJ, Iqbal J, Gunn J, Lawford P, Hoekstra AG. 2014 Endothelial repair process and its relevance to longitudinal neointimal tissue patterns: comparing histology with in silico modelling. *J. R. Soc. Interface* **11**, 20140022. (doi:10.1098/rsif.2014.0022)

37. Zun PS, Anikina T, Svitenkov A, Hoekstra AG. 2017 A comparison of fully-coupled 3D in-stent restenosis simulations to in-vivo data. *Front. Physiol.* **8**, 1–12. (doi:10.3389/fphys.2017.00284)

38. Zun PS, Narracott AJ, Chiastra C, Gunn J, Hoekstra AG. 2019 Location-specific comparison between a 3D in-stent restenosis model and micro-CT and histology data from porcine in vivo experiments. *Cardiovasc. Eng. Technol.* **10**, 568–582. (doi:10.1007/s13239-019-00431-4)

39. Boyle CJ, Lennon AB, Early M, Kelly DJ, Lally C, Prendergast PJ. 2010 Computational simulation methodologies for mechanobiological modelling: a cell-centred approach to neointima development in stents. *Philos. Trans. R. Soc. A Math. Phys. Eng. Sci.* **368**, 2919–2935. (doi:10.1098/rsta.2010.0071)

40. Boyle CJ, Lennon AB, Prendergast PJ. 2011 In silico prediction of the mechanobiological response of arterial tissue: application to angioplasty and stenting. *J. Biomech. Eng.* **133**, 081001. (doi:10.1115/1.4004492)

41. Zahedmanesh H, Van Oosterwyck H, Lally C. 2014 A multi-scale mechanobiological model of

in-stent restenosis: deciphering the role of matrix metalloproteinase and extracellular matrix changes. *Comput. Methods Biomech. Biomed. Engin.* **17**, 813–828. (doi:10.1080/10255842.2012.716830)

42. Nolan DR, Lally C. 2018 An investigation of damage mechanisms in mechanobiological models of in-stent restenosis. *J. Comput. Sci.* **24**, 132–142. (doi:10.1016/j.jocs.2017.04.009)

43. Li S, Lei L, Hu Y, Zhang Y, Zhao S, Zhang J. 2019 A fully coupled framework for in silico investigation of in-stent restenosis. *Comput. Methods Biomech. Biomed. Engin.* **22**, 217–228. (doi:10.1080/10255842.2018.1545017)

44. Schillinger M, Exner M, Mlekusch W, Rumpold H, Ahmadi R, Sabeti S, Haumer M, Wagner O, Minar E. 2002 Vascular inflammation and percutaneous transluminal angioplasty of the femoropopliteal artery: association with restenosis. *Radiology* **225**, 21–26. (doi:10.1148/radiol.2251011809)

45. Cipollone F *et al.* 2001 Elevated circulating levels of monocyte chemoattractant protein-1 in patients with restenosis after coronary angioplasty. *Arterioscler. Thromb. Vasc. Biol.* **21**, 327–334. (doi:10.1161/01.ATV.21.3.327)

46. Stefano GT, Mehanna E, Parikh SA. 2013 Imaging a spiral dissection of the superficial femoral artery in high resolution with optical coherence tomography-seeing is believing. *Catheter. Cardiovasc. Interv. Off. J. Soc. Card. Angiogr. Interv.* **81**, 568–572. (doi:10.1002/ccd.24292)

47. Nikishova A, Veen L, Zun P, Hoekstra AG. 2018 Uncertainty quantification of a multiscale model for in-stent restenosis. *Cardiovasc. Eng. Technol.* **9**, 761–774. (doi:10.1007/s13239-018-00372-4)

48. Ramasamy A *et al.* 2019 Reliable in vivo intravascular imaging plaque characterization: A challenge unmet. *Am. Heart J.* **218**, 20–31. (doi:10.1016/j.ahj.2019.07.008)

49. Iida O *et al.* 2011 Timing of the restenosis following nitinol stenting in the superficial femoral artery and the factors associated with early and late restenoses. *Catheter. Cardiovasc. Interv. Off. J. Soc. Card. Angiogr. Interv.* **78**, 611–617. (doi:10.1002/ccd.23064)

Table captions

Table 1. Arterial wall dimensions adopted for the agent-based model (ABM) construction.

Table 2. Agent-based model (ABM) parameters.

Table 3. Calibrated agent-based model (ABM) parameters.

Figure captions

Figure 1. Multiscale computational framework. Starting from the patient-specific inputs, the framework (dashed red box) simulates arterial wall remodeling and in-stent restenosis (ISR) along 1 simulated month and generates as output a three-dimensional (3D) model of arterial lumen geometry at 1 month of follow-up. The framework consists of 2 modules, namely (i) the hemodynamics module at the tissue-seconds scale, in which the 3D artery model is meshed and the computational fluid dynamics (CFD) simulation is performed to compute the wall shear stress (WSS), and (ii) the tissue remodeling module at the cell-days scale, in which an agent-based model (ABM) simulates cellular dynamics and arterial wall remodeling, and an updated 3D arterial lumen geometry is reconstructed from the ABM outputs.

Figure 2. Monocyte gene expression data of the 14 patients. The gene expression (GE) of 3 out of 34 clusters that were found to be significantly differentially expressed between success and failure groups are shown. Each grey curve represents a patient's gene profile of the specific cluster (average of the patient's genes belonging to the cluster), with the red ones referred to the patient selected for the application of the multiscale framework. The black curves are the average curves of all the patient's curves. All the gene expression curves were log2-transformed, namely the displayed value of gene expression was computed as $GE(t) = log_2\left(\frac{v(t)}{v(t0)}\right)$, where *v(t)* is the measured gene expression level at time *t* and *v(t0)* is the pre-operative gene expression level.

Figure 3. A) Patient-specific model of a superficial femoral artery (SFA) treated with the EverFlex stent at the Malcom Randall VA Medical Center (Gainesville, FL, USA). The model includes a small portion of the common femoral artery (CFA) and the profunda femoris artery (PFA). B) Detail of the polyhedral computational fluid dynamics (CFD) mesh of the inlet and stented portion. C) CFD model, with the applied boundary conditions and the resulting wall shear stress (WSS) contour map. In the stented portion, cross-sectional planes (1-9) were selected (1 every 2 stent rings) for the subsequent agent-based analysis. D) Agent-based model (ABM) of plane 5 and detail on the hexagonal grid.

Figure 4. A) Generic inflammatory curve, inspired from literature [24]. B) Example of gene expression-based input (*GEinput*) of the agent-based model (ABM). This curve was obtained with a value of p_{ge} = -3.854.

Figure 5. Results of the preliminary sensitivity analysis. Partial rank correlation coefficients (PRCCs) between the ABM parameters and (A) the 1-month lumen area, (B) extracellular matrix (ECM) intimal content and (C) smooth muscle cell (SMC) intimal content. To compute the PRCCs, the average ABM outputs obtained from the three repetitions (run for each parameter combination to account for stochasticity) were considered. PRCCs range from -1 to +1, with negative PRCCs corresponding to a negative correlation and positive PRCCs to a positive correlation. (*) Significant PRCC, $p < 0.05$.

Figure 6. Samples used for the construction of the surrogate models. The grey box plots represent the distribution of the patient's lumen area of the stented portion at time 0 (T0) and at 1 month (1M-p). The red box plots represent the distribution of the 1-month lumen area of the stented portion obtained from

60 simulated cases and ordered according to the absolute difference from the patient 1-month lumen area (1M-p), considering the median values. The blue box plots represent the distributions of the 1-month normalized intimal extracellular matrix / smooth muscle cell ratio (ECM/SMC_{ratio_int}) obtained from the 60 simulated cases.

Figure 7. Surrogate model validation. A) Leave-one-out predicted values of the 1-month lumen area and normalized intimal extracellular matrix / smooth muscle cell ratio (ECM/SMC_{ratio_int}) in function of the corresponding simulated values. B) Predicted values of the 1-month lumen area and normalized ECM/SMC_{ratio_int} in function of the corresponding simulated values for 10 additional cases (validation data set).

Figure 8. Parameter exploration. Predicted values of the 1-month lumen area and normalized intimal extracellular matrix / smooth muscle cell ratio (ECM/SMC_{ratio_int}) by varying three parameters at the time while maintaining the others at their half-range values. A) Predicted 1-month lumen area (colored variable) at the variation of the parameters associated with the hemodynamic input *WSSinput* (α_2, α_5, Amp). B) Predicted 1-month lumen area (colored variable) at the variation of the parameters associated with the gene expression input *GEinput* (α_3, α_6, p_{ge}). C) Predicted normalized ECM/SMC_{ratio_int} (colored variable) at the variation of the parameters associated with the hemodynamic input *WSSinput* (α_2, α_5, Amp). D) Predicted normalized ECM/SMC_{ratio_int} (colored variable) at the variation of the parameters associated with the gene expression input *GEinput* (α_3, α_6, p_{ge}).

Figure 9. Results of the calibrated framework for 3 explanatory planes of the stented region of the patient-specific superficial femoral artery model. A) Wall shear stress (WSS) contour of the stented portion (left) and temporal evolution of the agent-based models (ABM) of 3 explanatory planes (plane 1, plane 5 and plane 9) along 1 simulated month (day 0, day 10, day 20 and day 30). For each ABM plane, the results were retrieved from 1 out of 3 ABM simulations, namely the one presenting the lumen configuration minimizing the root mean square deviation from the average one, as detailed in Section 2.1.5. B) Normalized lumen area over time for planes 1 (green), 5 (yellow) and 9 (violet). The dashed black line represents the (not scaled) gene expression-based input (*GEinput*), also reported in Fig. 4B. C) Normalized area over time of the intima (solid line), media (dashed line) and adventitia (dotted line) layers for the plane 1 (green), 5 (yellow) and 9 (violet). D) Normalized intimal content of smooth muscle cells (SMC) (solid line) and extracellular matrix (ECM) (dashed line) over time for the plane 1 (green), 5 (yellow) and 9 (violet). E) Normalized intimal ECM/SMC ratio (ECM/SMC_{ratio_int}) over time for the plane 1 (green), 5 (yellow) and 9 (violet).

Figure 10. Geometry reconstruction of the stented region of the superficial femoral artery model at 1 month. A) 1-month ABM outputs of the selected simulations for the 9 planes within the stented region. B) Lumen contours extracted from the 1-month ABM outputs of the 9 planes. C) Lumen surface reconstruction.

Figure 11. Evaluation of the model prediction. A) Left: Lumen surface of the stented portion of the patient-specific superficial femoral artery model immediately after the intervention (T0) reconstructed from computed tomography (CT) images; center: lumen surface of the stented portion of the patient-

specific model at 1 month, reconstructed from CT (1M-patient); right: lumen surface of the stented portion at 1-month, obtained from the framework (1M-model). B) Boxplots of the lumen area of the stented portion immediately after the intervention (T0), at 1 month of the patient's case (1M-patient) and at 1 month of the calibrated model case (1M-model). Kruskal-Wallis test with multiple comparison was used to compare the 3 groups. * p-value < 0.05 (p-value correction through Tukey-Kramer method).

Tables

Table 1. Arterial wall dimensions adopted for the agent-based model (ABM) construction.

Dimension [Ref]	Value	Artery
Wall thickness / Lumen diameter [21]	0.22	Human popliteal artery
Intima thickness / Wall thickness [22]	0.18	Human common femoral artery
Media thickness / Wall thickness [22]	0.52	Human common femoral artery
Adventitia thickness / Wall thickness [22]	0.30	Human common femoral artery

Table 2. Agent-based model (ABM) parameters.

Parameter	Meaning	Range
α_2	Multiply *WSSinput* in SMC probability	[0; 0.1]
α_3	Multiply *GEinput* in SMC probability	[0; 1.7]
α_5	Multiply *WSSinput* in ECM probability	[0; 0.1]
α_6	Multiply *GEinput* in ECM probability	[0; 1.77]
L_1	Slope of D	[-25; -5.5]
L_2	Half decay of D	[0.4;0.6]
Amp	Amplitude of the cosine function representing the diffusion of D in the intima	[0.013; 0.13]
p_{ge}	Slope of the weights of gene expression	[-6; -2.5]

WSSinput: wall shear stress input; *GEinput*: gene expression input; SMC: smooth muscle cell; ECM: extracellular matrix; D: variable representing the level of endothelial dysfunction.

Table 3. Calibrated agent-based model (ABM) parameters.

α_2	α_3	α_5	α_6	Amp	p_{ge}
0.06	1.614	0.019	0.928	0.065	-3.854

Figures

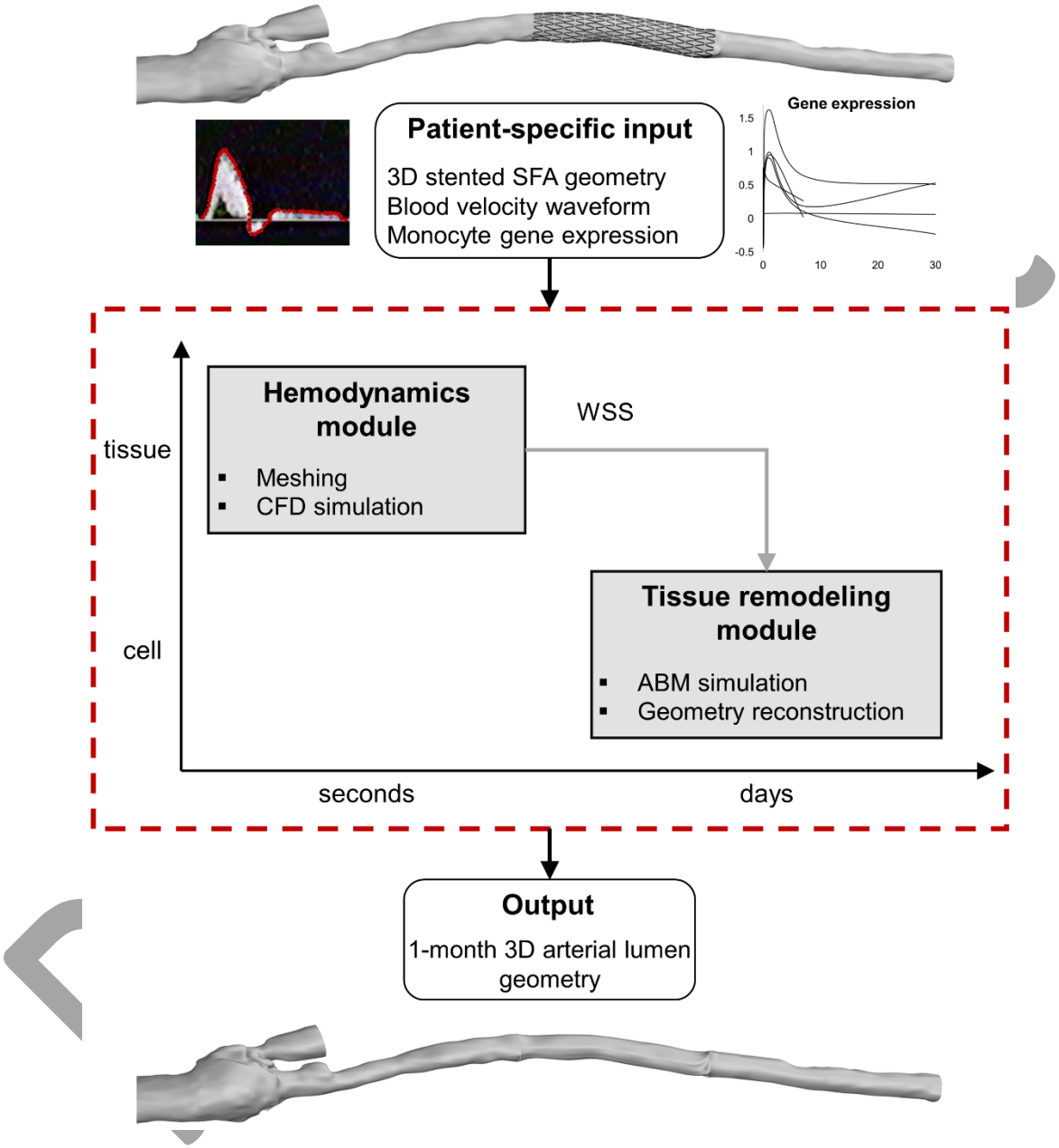

Figure 1. Multiscale computational framework. Starting from the patient-specific inputs, the framework (dashed red box) simulates arterial wall remodeling and in-stent restenosis (ISR) along 1 simulated month and generates as output a three-dimensional (3D) model of arterial lumen geometry at

1 month of follow-up. The framework consists of 2 modules, namely (i) the hemodynamics module at the tissue-seconds scale, in which the 3D artery model is meshed and the computational fluid dynamics (CFD) simulation is performed to compute the wall shear stress (WSS), and (ii) the tissue remodeling module at the cell-days scale, in which an agent-based model (ABM) simulates cellular dynamics and arterial wall remodeling, and an updated 3D arterial lumen geometry is reconstructed from the ABM outputs.

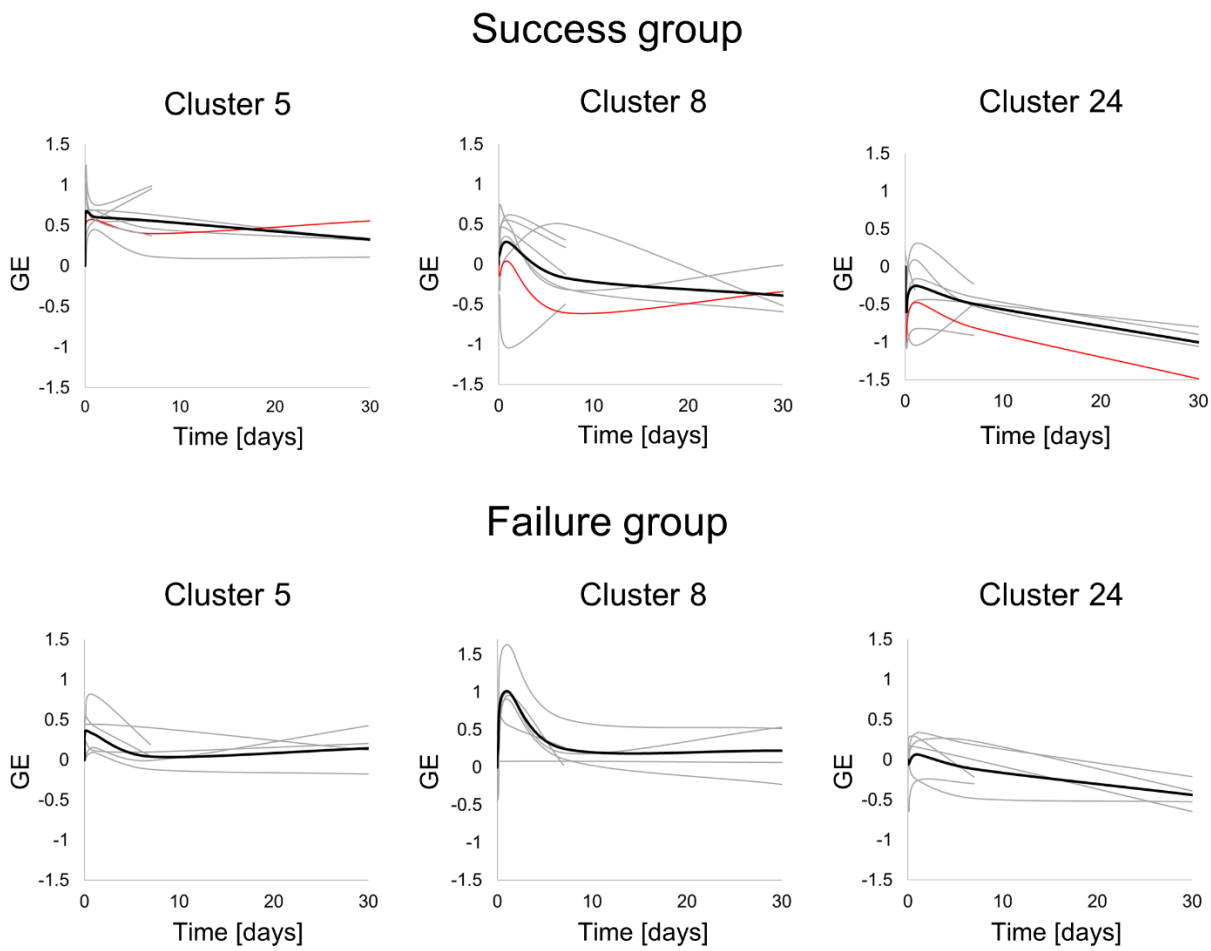

Figure 2. Monocyte gene expression data of the 14 patients. The gene expression (GE) of 3 out of 34 clusters that were found to be significantly differentially expressed between success and failure groups are shown. Each grey curve represents a patient's gene profile of the specific cluster (average of the patient's genes belonging to the cluster), with the red ones referred to the patient selected for the application of the multiscale framework. The black curves are the average curves of all the patient's curves. All the gene expression curves were log2-transformed, namely the displayed value of gene expression was computed as $GE(t) = log_2\left(\frac{v(t)}{v(t0)}\right)$, where *v(t)* is the measured gene expression level at time *t* and *v(t0)* is the pre-operative gene expression level.

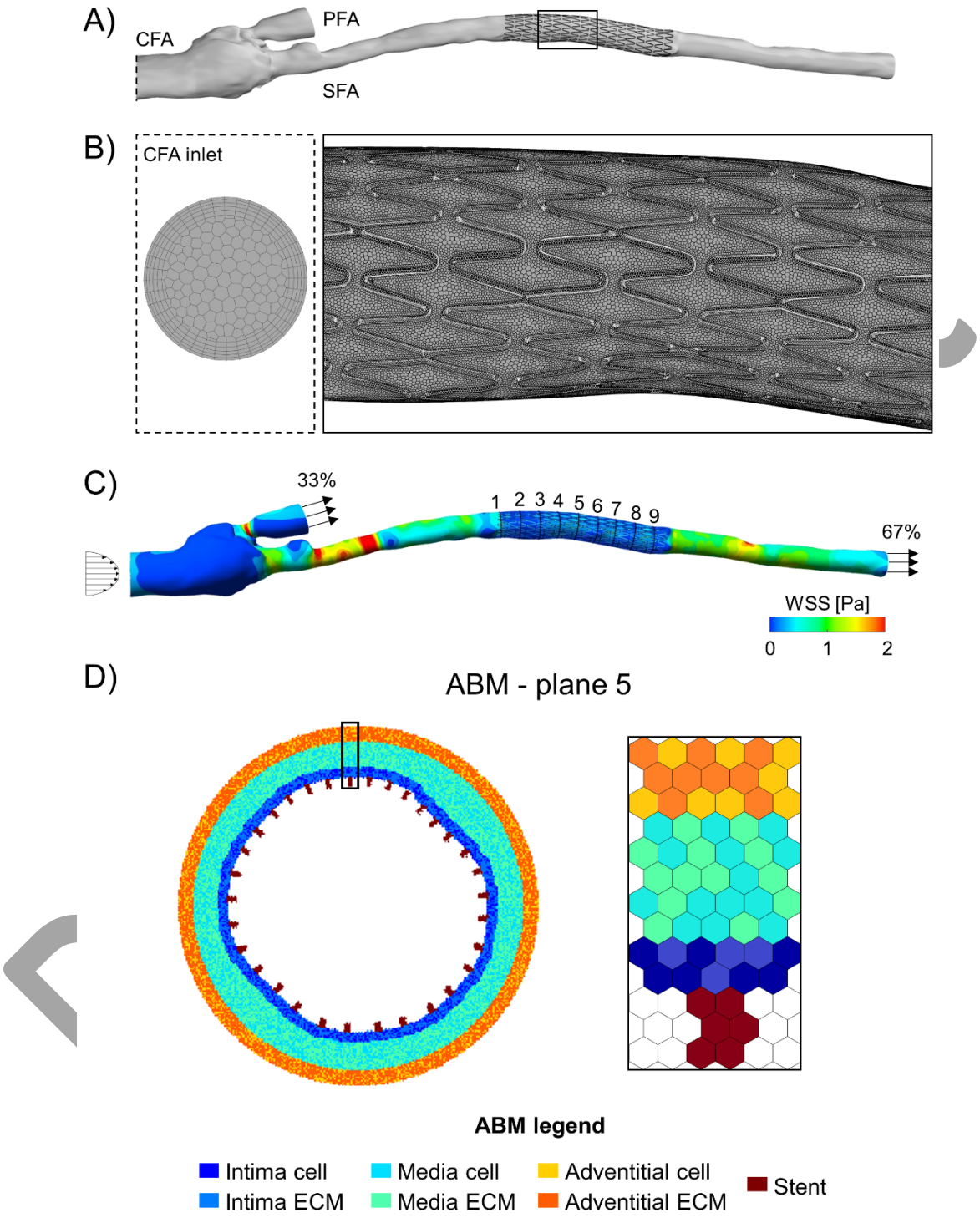

Figure 3. A) Patient-specific model of a superficial femoral artery (SFA) treated with the EverFlex stent at the Malcom Randall VA Medical Center (Gainesville, FL, USA). The model includes a small

portion of the common femoral artery (CFA) and the profunda femoris artery (PFA). B) Detail of the polyhedral computational fluid dynamics (CFD) mesh of the inlet and stented portion. C) CFD model, with the applied boundary conditions and the resulting wall shear stress (WSS) contour map. In the stented portion, cross-sectional planes (1-9) were selected (1 every 2 stent rings) for the subsequent agent-based analysis. D) Agent-based model (ABM) of plane 5 and detail on the hexagonal grid.

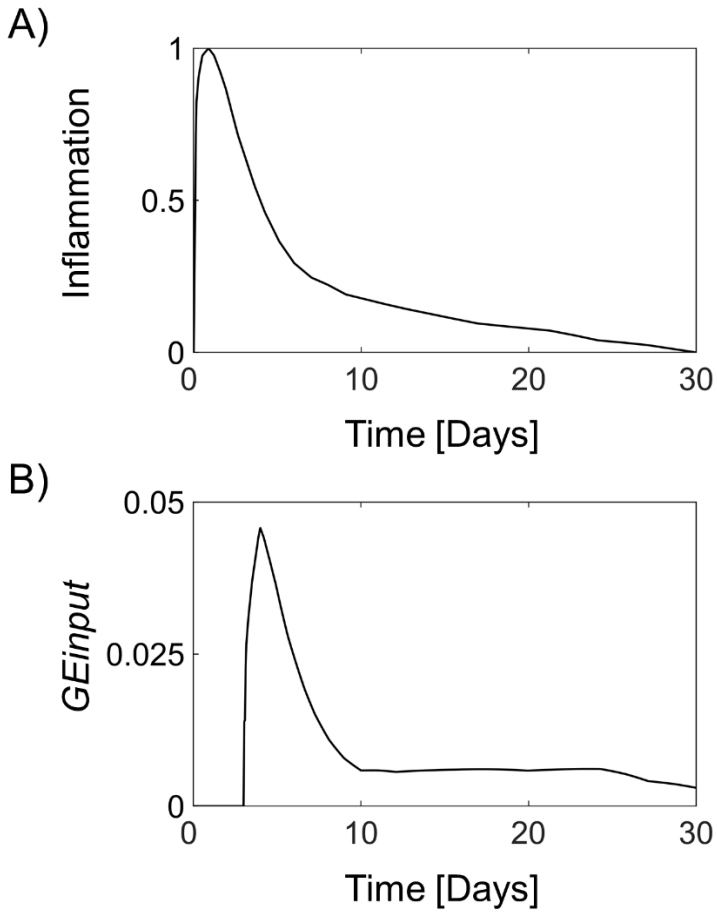

Figure 4. A) Generic inflammatory curve, inspired from literature [24]. B) Example of gene expression-based input (*GEinput*) of the agent-based model (ABM). This curve was obtained with a value of p_{ge} = -3.854.

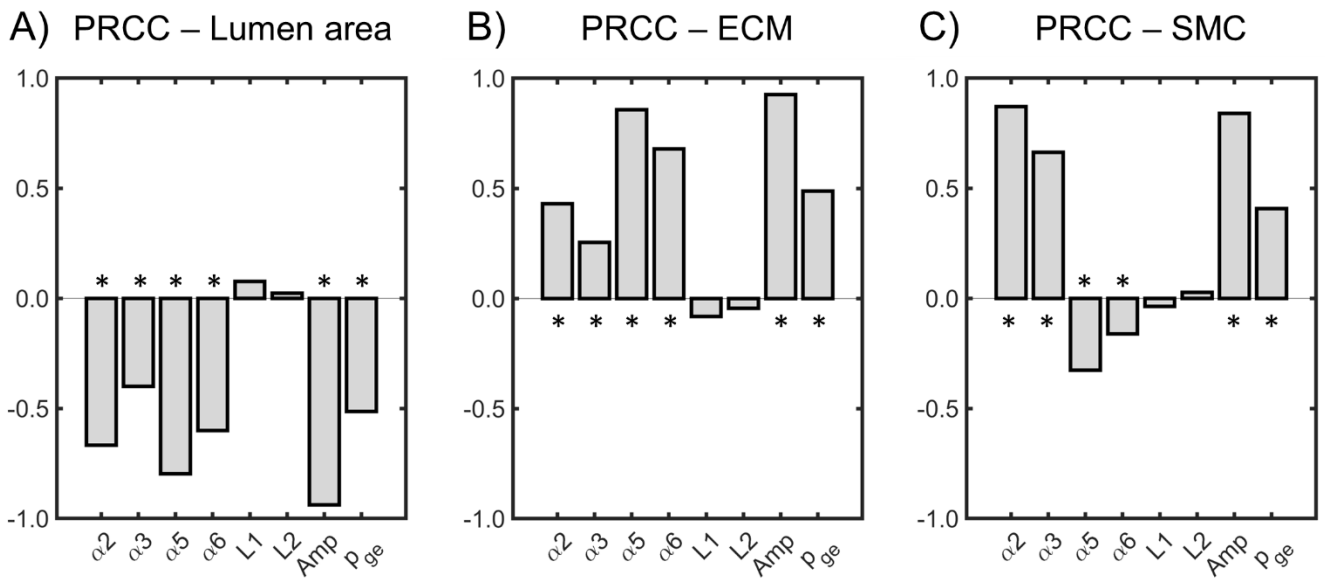

Figure 5. Results of the preliminary sensitivity analysis. Partial rank correlation coefficients (PRCCs) between the ABM parameters and (A) the 1-month lumen area, (B) extracellular matrix (ECM) intimal content and (C) smooth muscle cell (SMC) intimal content. To compute the PRCCs, the average ABM outputs obtained from the three repetitions (run for each parameter combination to account for stochasticity) were considered. PRCCs range from -1 to +1, with negative PRCCs corresponding to a negative correlation and positive PRCCs to a positive correlation. (*) Significant PRCC, $p < 0.05$.

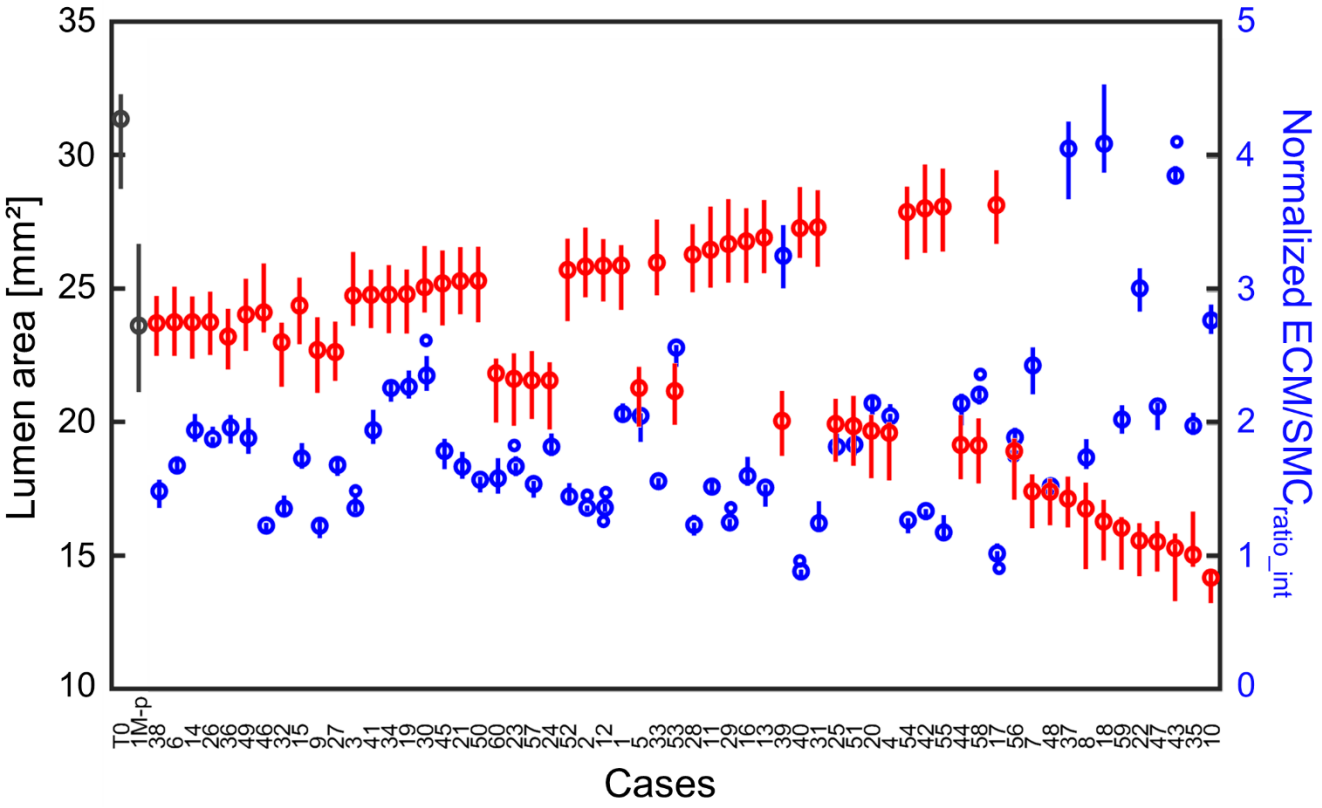

Figure 6. Samples used for the construction of the surrogate models. The grey box plots represent the distribution of the patient's lumen area of the stented portion at time 0 (T0) and at 1 month (1M-p). The red box plots represent the distribution of the 1-month lumen area of the stented portion obtained from 60 simulated cases and ordered according to the absolute difference from the patient 1-month lumen area (1M-p), considering the median values. The blue box plots represent the distributions of the 1-month normalized intimal extracellular matrix / smooth muscle cell ratio (ECM/SMC_{ratio_int}) obtained from the 60 simulated cases.

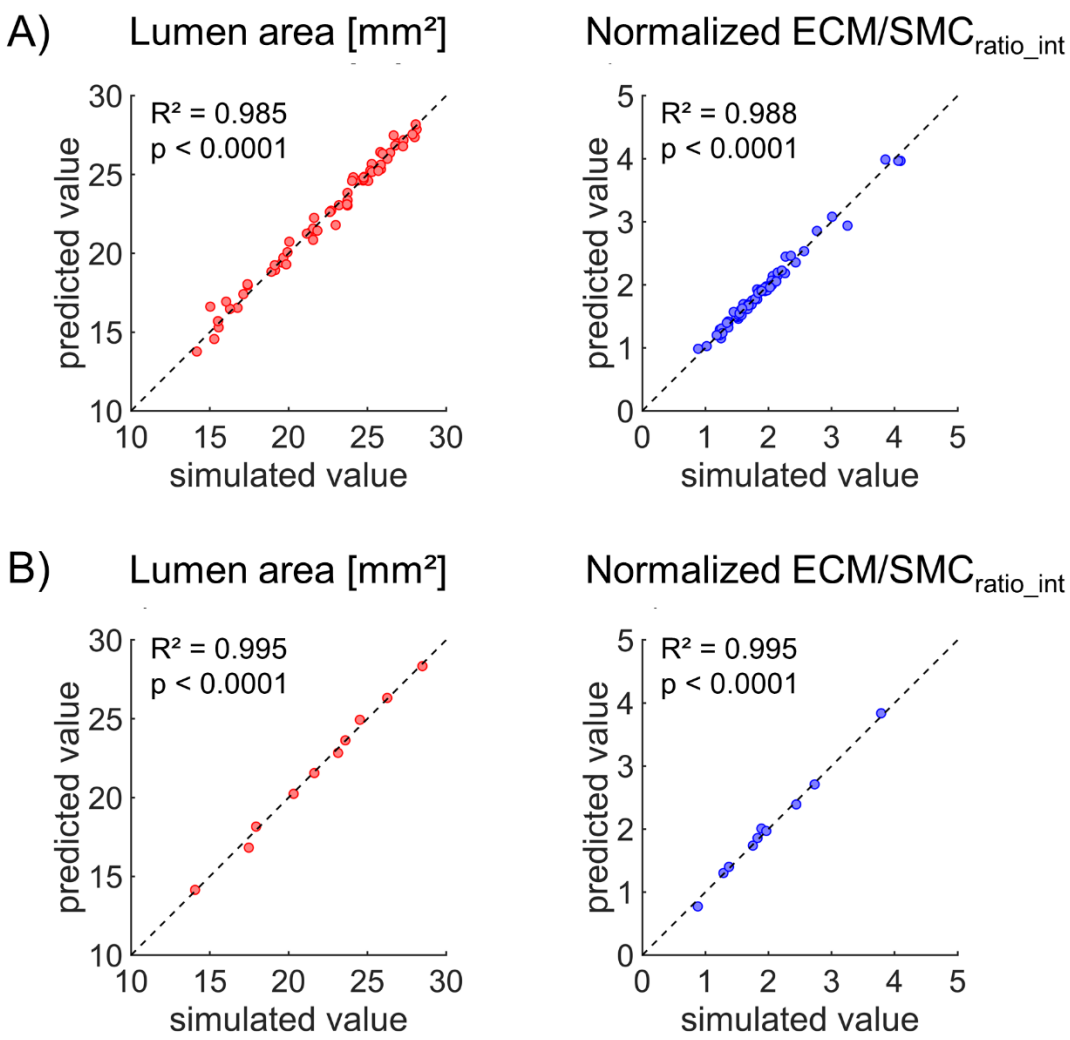

Figure 7. Surrogate model validation. A) Leave-one-out predicted values of the 1-month lumen area and normalized intimal extracellular matrix / smooth muscle cell ratio (ECM/SMC_{ratio_int}) in function of the corresponding simulated values. B) Predicted values of the 1-month lumen area and normalized ECM/SMC_{ratio_int} in function of the corresponding simulated values for 10 additional cases (validation data set).

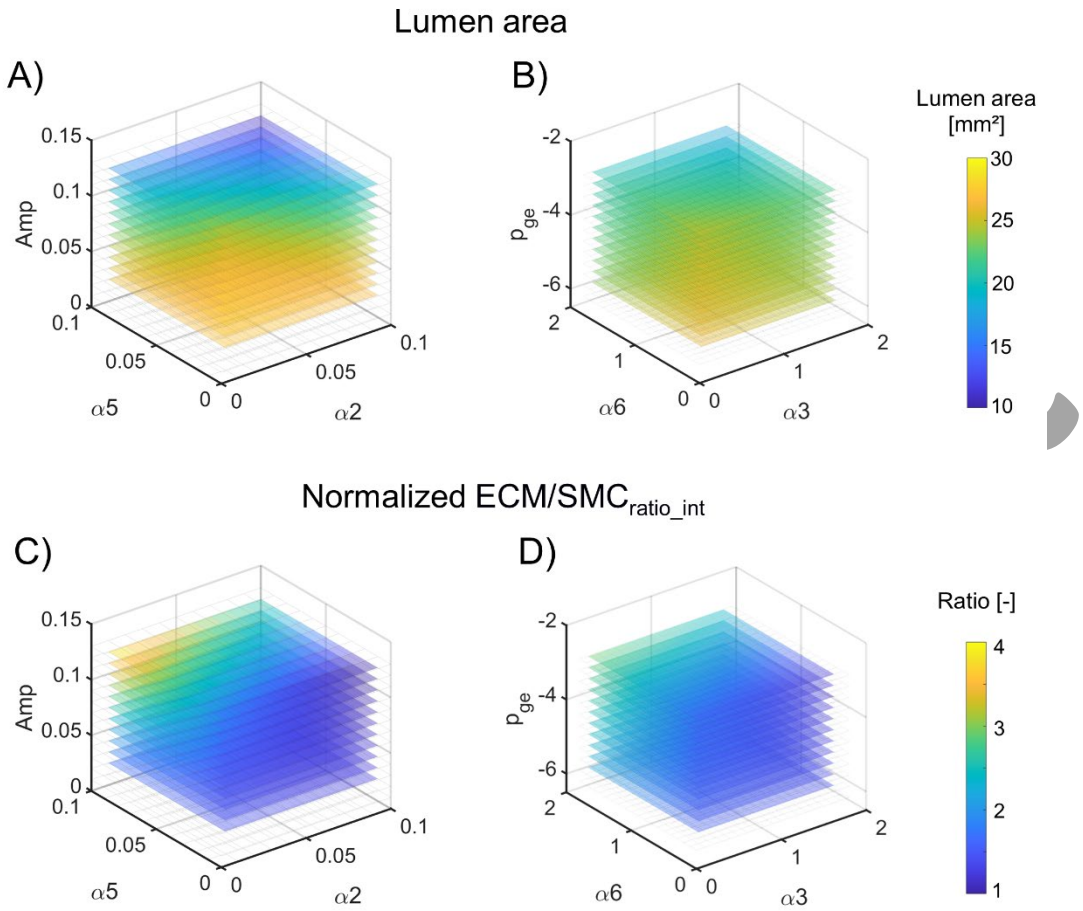

Figure 8. Parameter exploration. Predicted values of the 1-month lumen area and normalized intimal extracellular matrix / smooth muscle cell ratio (ECM/SMC$_{ratio_int}$) by varying three parameters at the time while maintaining the others at their half-range values. A) Predicted 1-month lumen area (colored variable) at the variation of the parameters associated with the hemodynamic input *WSSinput* (α_2, α_5, Amp). B) Predicted 1-month lumen area (colored variable) at the variation of the parameters associated with the gene expression input *GEinput* (α_3, α_6, p_{ge}). C) Predicted normalized ECM/SMC$_{ratio_int}$ (colored variable) at the variation of the parameters associated with the hemodynamic input *WSSinput* (α_2, α_5, Amp). D) Predicted normalized ECM/SMC$_{ratio_int}$ (colored variable) at the variation of the parameters associated with the gene expression input *GEinput* (α_3, α_6, p_{ge}).

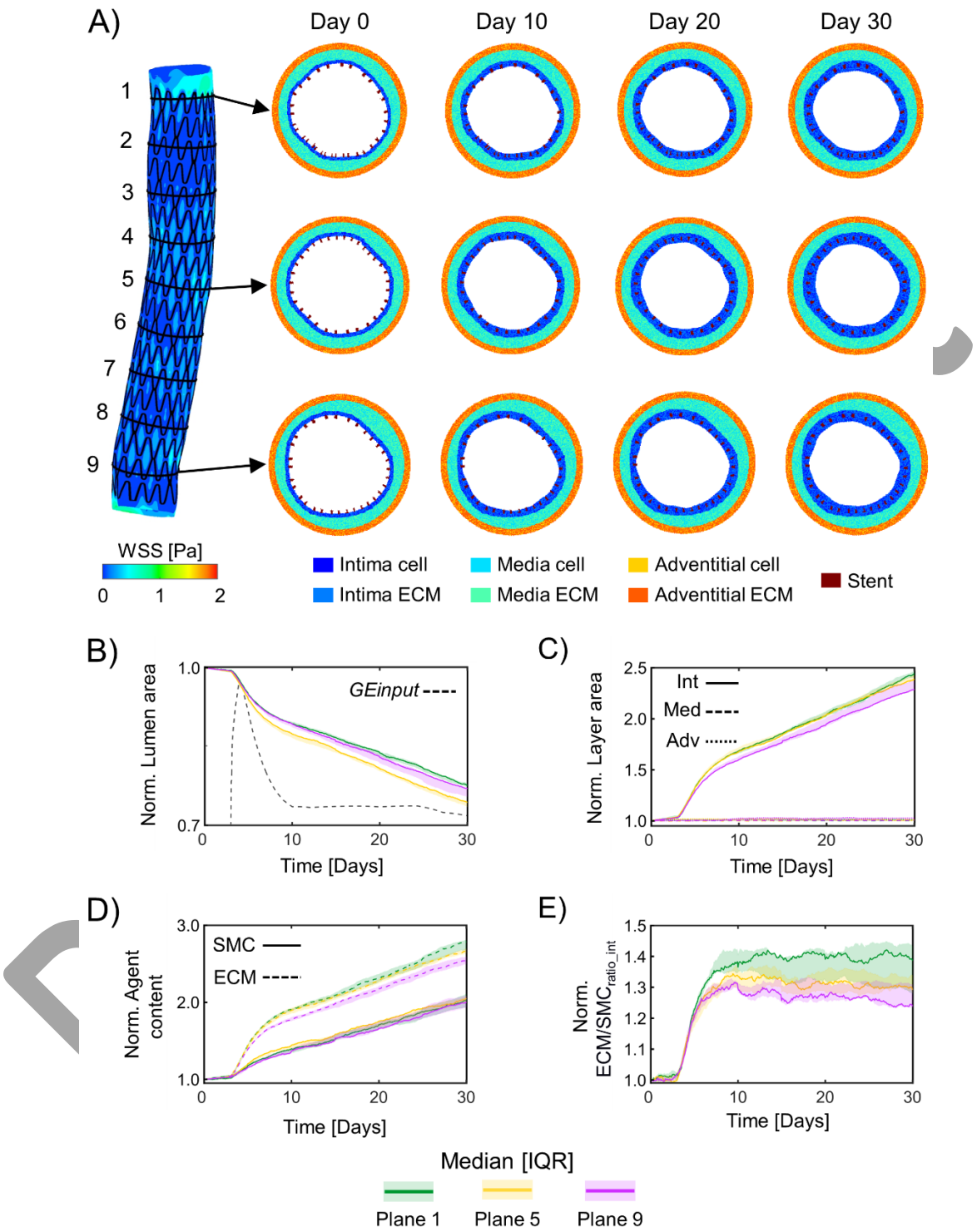

Figure 9. Results of the calibrated framework for 3 explanatory planes of the stented region of the patient-specific superficial femoral artery model. A) Wall shear stress (WSS) contour of the stented

portion (left) and temporal evolution of the agent-based models (ABM) of 3 explanatory planes (plane 1, plane 5 and plane 9) along 1 simulated month (day 0, day 10, day 20 and day 30). For each ABM plane, the results were retrieved from 1 out of 3 ABM simulations, namely the one presenting the lumen configuration minimizing the root mean square deviation, as detailed in Section 2.1.5. B) Normalized lumen area over time for planes 1 (green), 5 (yellow) and 9 (violet). The dashed black line represents the (not scaled) gene expression-based input (*GEinput*), also reported in Fig. 4B. C) Normalized area over time of the intima (solid line), media (dashed line) and adventitia (dotted line) layers for the plane 1 (green), 5 (yellow) and 9 (violet). D) Normalized intimal content of smooth muscle cells (SMC) (solid line) and extracellular matrix (ECM) (dashed line) over time for the plane 1 (green), 5 (yellow) and 9 (violet). E) Normalized intimal ECM/SMC ratio (ECM/SMC_{ratio_int}) over time for the plane 1 (green), 5 (yellow) and 9 (violet).

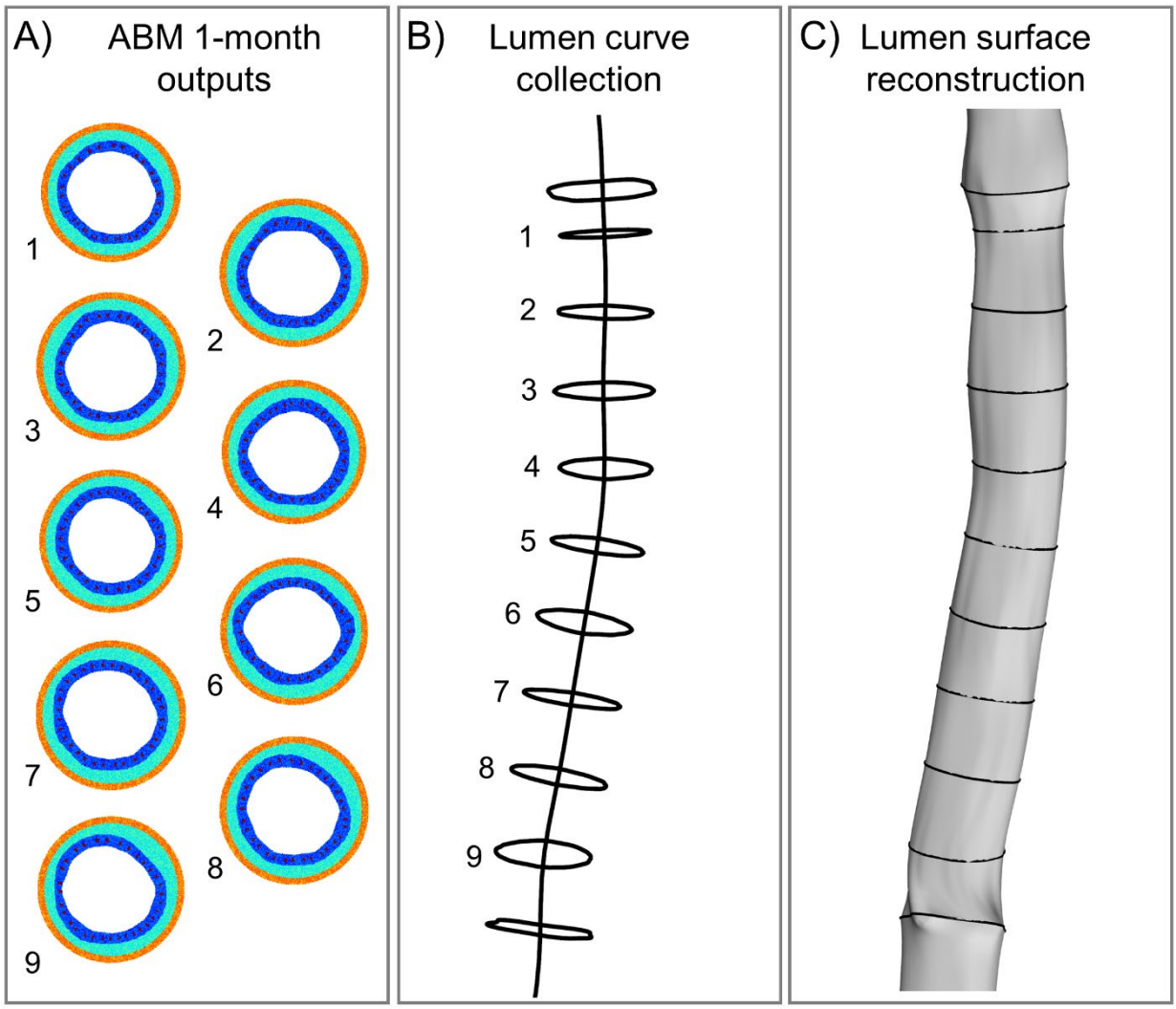

Figure 10. Geometry reconstruction of the stented region of the superficial femoral artery model at 1 month. A) 1-month ABM outputs of the selected simulations for the 9 planes within the stented region. B) Lumen contours extracted from the 1-month ABM outputs of the 9 planes. C) Lumen surface reconstruction.

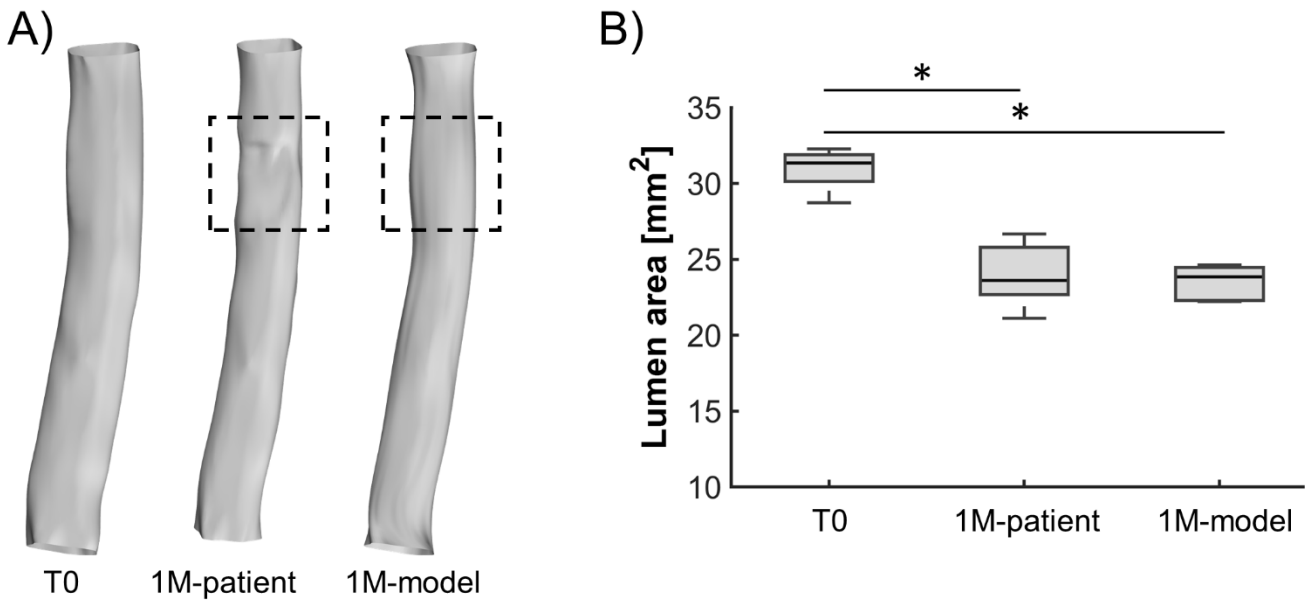

Figure 11. Evaluation of the model prediction. A) Left: Lumen surface of the stented portion of the patient-specific superficial femoral artery model immediately after the intervention (T0) reconstructed from computed tomography (CT) images; center: lumen surface of the stented portion of the patient-specific model at 1 month, reconstructed from CT (1M-patient); right: lumen surface of the stented portion at 1-month, obtained from the framework (1M-model). B) Boxplots of the lumen area of the stented portion immediately after the intervention (T0), at 1 month of the patient's case (1M-patient) and at 1 month of the calibrated model case (1M-model). Kruskal-Wallis test with multiple comparison was used to compare the 3 groups. * p-value < 0.05 (p-value correction through Tukey-Kramer method).